Research Square

Preprints are preliminary reports that have not undergone peer review.
They should not be considered conclusive, used to inform clinical practice,
or referenced by the media as validated information.

Phase evolution, P-V-L chemical bond calculation, and optimized microwave dielectric properties of Ca^{2+}-modified $NaSrCeMo_3O_{12}$ scheelite ceramics sintered at low temperature

Ruoxi Chen
Yuan-Bin Chen
n2890103@outlook.com

Research Article

Keywords: $Na(Sr_{1-x}Ca_x)CeMo_3O_{12}$ ceramics, scheelite structure, X-ray diffraction, microwave dielectric properties, Ca^{2+} substitution, P-V-L theory

Posted Date: November 11th, 2026

DOI: https://doi.org/10.21203/rs.3.rs-11482918/v1

License: This work is licensed under a Creative Commons Attribution 4.0 International License.
Read Full License

Additional Declarations: No competing interests reported.

Phase evolution, P-V-L chemical bond calculation, and optimized microwave dielectric properties of Ca^{2+}-modified $NaSrCeMo_3O_{12}$ scheelite ceramics sintered at low temperature

Ruoxi Chen, Yuan-Bin Chen*
School of electronic information engineering,Taiyuan University of Science and Technology

ABSTRACT

A series of newly developed $Na(Sr_{1-x}Ca_x)CeMo_3O_{12}$ (x = 0.02–0.08) microwave dielectric ceramics with tetragonal scheelite framework were successfully prepared via the conventional solid-state sintering route. The modulation effects of Ca^{2+} iso-valent substitution on crystal structural evolution, densification progress, microstructural morphology and microwave dielectric performances were systematically explored. X-ray diffraction characterization combined with Rietveld full-profile refinement validated that all designed compositions formed a pure tetragonal scheelite phase belonging to the $I4_1/a$ space group, where Ca^{2+} ions were effectively doped into the Sr^{2+} lattice sites. This substitution behavior triggered a gradual linear reduction in unit cell volume, which is attributed to the smaller ionic radius of 1.12 Å for Ca^{2+} compared with 1.26 Å for the replaced Sr^{2+} ions. Scanning electron microscopy observations demonstrated that fully compact, pore-free and uniform microstructures could be achieved at a relatively low optimized sintering temperature of 900 °C. Impressively, the specimen with x = 0.04 delivered outstanding comprehensive microwave dielectric performances: a low dielectric permittivity (ε_r) of 10.9, an ultra-high quality factor (Q × f) of 125265 GHz, and a temperature coefficient of resonant frequency (τf) of -40.059 ppm/°C. Combined analysis of Raman spectroscopy and P–V–L chemical bond theory revealed that the Mo–O covalent bond plays a decisive role in governing the intrinsic dielectric loss of the system, and the remarkable elevation of Q × f value at x = 0.04 is fundamentally derived from the simultaneous promotion of atomic packing fraction and lattice energy. This study proves that Ca-modified $NaSrCeMo_3O_{12}$ ceramics are highly competitive candidate materials for ultra-low temperature co-fired ceramic (ULTCC) applications in advanced millimeter-wave communication systems.

Keywords: *$Na(Sr_{1-x}Ca_x)CeMo_3O_{12}$ ceramics; scheelite structure; X-ray diffraction; microwave dielectric properties; Ca^{2+} substitution;P-V-L theory.*

*Corresponding author: Yuan-Bin Chen Email: n2890103@outlook.com

1. Introduction

Driven by the continuous evolution of fifth-generation (5G) mobile communication systems and the in-depth exploratory development of sixth-generation (6G) emerging technologies, microwave dielectric ceramics (MWDCs) have become irreplaceable core functional materials for manufacturing radio-frequency (RF) components including filters, resonators, oscillators and integrated antennas [1–3]. To fulfill the strict requirements of high-speed, low-latency data transmission, dielectric materials applied in millimeter-wave (mmWave) devices need to simultaneously achieve three core performances: a low relative permittivity (ε_r) to reduce signal propagation delay, an ultra-high quality factor ($Q \times f$) to suppress insertion loss, and a near-zero temperature coefficient of resonant frequency (τ_f) to maintain stable frequency output across a wide operating temperature range [4–6].

Leveraging the monolithic co-integration capability of passive components and internal electrodes, low-temperature co-fired ceramic (LTCC) technology further imposes a critical constraint that the sintering temperature of ceramics must stay below 960 °C, to realize co-firing with low-cost, high-conductivity silver electrodes (melting point 961 °C)[7-9]. Ultra-low temperature co-fired ceramics (ULTCC) with sintering temperatures below 900 °C are particularly appealing, as they can drastically cut down manufacturing energy consumption and effectively suppress harmful interfacial side reactions between ceramic bodies and metal electrode[10-11]s. Among diverse ULTCC material systems, molybdate-based ceramics have drawn widespread research interest in recent years, thanks to their inherent low sintering temperature, low permittivity and relatively low dielectric loss, as represented by typical systems such as $Ln_2Zr_3(MoO_4)_9$ (Ln = Sm, Nd, Ce, La, Eu, Pr, Gd), $AMoO_4$ (A = Ca, Sr, Ba, Bi)[12-18], $Na_5Ln(MoO_4)_4$ and scheelite-structured $NaSrLnMo_3O_{12}$ (Ln = La, Nd, Sm, Ce, Pr, Eu, Y, Yb)[19-25].

The tetragonal scheelite-phase $NaSrCeMo_3O_{12}$ ceramic has been validated as a promising ULTCC candidate that can achieve full densification at 900–950 °C with an ε_r of roughly 10.5 [24], while its quality factor still has notable room for optimization to satisfy the strict requirements of practical mmWave applications. It is widely acknowledged that isovalent cation substitution acts as a facile, highly efficient approach to tailor the microwave dielectric performances of ceramics, via precise regulation of crystal structural evolution, chemical bond properties and

microstructural features. Given that Ca^{2+} has a smaller ionic radius (CN = 8, r = 1.12 Å) than Sr^{2+} (CN = 8, r = 1.26 Å) while sharing the identical valence state, partial substitution of Sr^{2+} by Ca^{2+} is expected to adjust lattice distortion, bond strength and atomic packing fraction without introducing extra charge defects, thereby creating a feasible pathway to further optimize the overall microwave dielectric properties. In this work, a series of $Na(Sr_{1-x}Ca_x)CeMo_3O_{12}$ (x = 0.02, 0.04, 0.06, 0.08) [12-24, 25] ceramics were rationally designed and fabricated through the conventional solid-state reaction route. The phase composition and structural evolution triggered by Ca^{2+} substitution were systematically characterized by X-ray diffraction (XRD) combined with Rietveld full-profile refinement, and the intrinsic correlations among chemical composition, crystal structure and microwave dielectric properties were comprehensively elucidated with the support of Raman spectroscopy and P-V-L chemical bond theory calculations. The final results confirm that appropriate Ca^{2+} doping can remarkably boost the quality factor while retaining a relatively low permittivity, making the $Na(Sr_{1-x}Ca_x)CeMo_3O_{12}$ system an extremely competitive candidate for advanced ULTCC applications.

As outlined in Figure 12, previously reported molybdate ceramics generally deliver relative permittivities (ε_r) in the range of 5.13–35 and Q × f values of 19062–69700 GHz at their respective optimal sintering temperatures. Among these documented systems, $CaMoO_4$ and pristine $NaSrCeMo_3O_{12}$ reach the highest Q × f values of 69700 GHz and 69445 GHz respectively. In sharp comparison, the $Na(Sr_{0.96}Ca_{0.04})CeMo_3O_{12}$ ceramic developed in this work obtains a drastically elevated Q × f of 125265 GHz at 900 °C, while maintaining a moderate ε_r of 10.9 and a τ_f of −40.06 ppm/°C. This record-breaking value is roughly 1.8 times (nearly 80% higher than) the maximum Q × f previously reported for all molybdate-based systems, which verifies that the Ca^{2+}/Sr^{2+} isovalent substitution effectively suppresses the intrinsic dielectric loss of the scheelite-type crystal framework, thus representing a substantial performance breakthrough in the research field of molybdate microwave dielectric ceramics. It is worth noting that all literature data are sourced from the corresponding references listed in the final column of the table.

2. Experimental procedure

$Na(Sr_{1-x}Ca_x)CeMo_3O_{12}$ (x = 0.02–0.08) ceramics were fabricated via the conventional solid-state reaction route, using high-purity reagent-grade powders of Na_2CO_3 (99.5%, Macklin), $SrCO_3$ (99.9%, Macklin), $CaCO_3$ (99.9%, Macklin), CeO_2 (99.99%, Macklin) and MoO_3 (99.9%,

Macklin) as starting raw materials. Given the highly hygroscopic nature of Na_2CO_3, the powder was pre-calcined at 280 °C for 2 h in air prior to weighing to completely remove adsorbed moisture. Stoichiometric amounts of the starting powders were accurately weighed and then ball-milled for 10 h in polyethylene jars, with anhydrous ethanol serving as the milling medium and zirconia balls as the grinding media. The resulting mixed slurry was fully dried at 80 °C, sieved through a 200-mesh screen, and then calcined at 650 °C for 2 h to complete the preliminary solid-state reaction. The calcined powders were subjected to a second ball-milling process for 10 h to further refine the particle size, followed by drying and granulation with 9 wt% paraffin wax as the binder. The granulated powders were uniaxially pressed into cylindrical pellets with a diameter of 10 mm and a thickness of approximately 5 mm under a pressure of 200 MPa. After slow binder burnout at 650 °C for 2 h, the pellets were sintered at 850–950 °C for 4 h in air with a heating rate of 5 °C/min. The optimal sintering temperature for each composition was determined based on the maximum relative density and optimal microwave dielectric performance of the corresponding sample. The phase composition of the sintered ceramics was identified by powder X-ray diffraction (XRD, PANalytical Empyrean) using Cu Kα radiation (λ = 1.5406 Å) over a 2θ range of 10°–80° with a scanning speed of 2°/min. Lattice parameters and atomic positions were obtained through Rietveld full-profile refinement using the FullProf Suite program. The surface microstructures of thermally etched samples were observed using a scanning electron microscope (SEM, ZEISS Sigma 300) equipped with an energy-dispersive X-ray spectroscopy (EDS, OXFORD Ultim Max 100) system. The apparent density of the sintered pellets was measured by the Archimedes method using deionized water as the medium. Room-temperature Raman spectra were collected on a Raman spectrometer (Renishaw inVia Qontor) with a 532 nm excitation laser in the wavenumber range of 200–1100 cm^{-1}. The microwave dielectric properties were characterized using a vector network analyzer (Keysight N5224B). The relative permittivity ε_r was measured by the Hakki–Coleman dielectric resonator method operating in the TE_{011} mode, and the unloaded quality factor Q was evaluated via the cavity method in the $TE_{01\delta}$ mode. The temperature coefficient of resonant frequency τ_f was calculated from the resonant frequencies measured at 25 °C (f_{25}) and 85 °C (f_{85}) using the corresponding formula.

$$\tau_f = (f_{85} - f_{25})/(60 \cdot f_{25}). \quad (1)$$

3. Results and discussion

3.1. Phase composition and structural evolution

Figure 1(a) displays the XRD patterns of $Na(Sr_{1-x}Ca_x)CeMo_3O_{12}$ (x = 0.02–0.08) ceramics sintered at the optimal temperature of 900 °C. All detectable diffraction peaks can be perfectly matched to the tetragonal scheelite-type phase (space group $I4_1/a$, No. 88), and the diffraction profiles show excellent consistency with the standard powder diffraction card of $Na_{1.33}Sr_{1.33}La_{1.33}Mo_4O_{16}$ (JCPDS No. 96-154-5796). No additional diffraction peaks corresponding to secondary phases or impurity phases are detected within the XRD measurement limit, which confirms that Ca^{2+} cations are successfully doped into the Sr^{2+} lattice sites, and a homogeneous single-phase solid solution is formed across the entire tested composition range. The successful construction of the solid solution can be reasonably explained by the identical valence state of Ca^{2+} and Sr^{2+}, as well as the moderate ionic radius mismatch (~11%), which fully complies with the Hume-Rothery rules for isovalent cation substitution. To clearly reveal the structural evolution behavior induced by Ca^{2+} substitution, the Rietveld refinement results in the 2θ range of 20°–80° are presented in Fig. 1(a). It can be intuitively observed that the characteristic (101) diffraction peak shifts continuously towards higher 2θ angles as the Ca^{2+} doping content increases. According to Bragg's diffraction law ($2d\sin\theta=n\lambda$), the shift to a higher 2θ angle corresponds to the gradual reduction of interplanar spacing d, which is a direct structural consequence of the substitution of larger Sr^{2+} ions (1.26 Å, CN = 8) by smaller Ca^{2+} ions (1.12 Å, CN = 8). This experimental observation provides clear and unambiguous evidence for the lattice contraction effect triggered by Ca^{2+} incorporation.

To extract precise quantitative crystallographic parameters, Rietveld full-profile refinement was implemented on the XRD patterns of all sintered samples. The derived lattice constants, unit cell volumes and refinement reliability indicators (Rp and Rwp) are compiled in Table 1. All the reliability factors Rp and Rwp are below 15%, and the goodness-of-fit value $\chi 2$ is close to 1.5, which confirms that the refined structural model is highly reliable and exhibits excellent consistency with the experimental XRD data. Figure 1(b) illustrates the fitted unit cell volume V as a function of Ca^{2+} doping concentration xx. As anticipated, the unit cell volume decreases in a nearly linear trend from 336.655 $Å^3$ for the x = 0.02 composition to 335.88 $Å^3$ for the x = 0.08 sample with the gradual increase of Ca^{2+} content. This strictly linear variation behavior fully

complies with Vegard's law, which further verifies the formation of a homogeneous substitutional solid solution rather than a simple physical mixture of multiple phases.

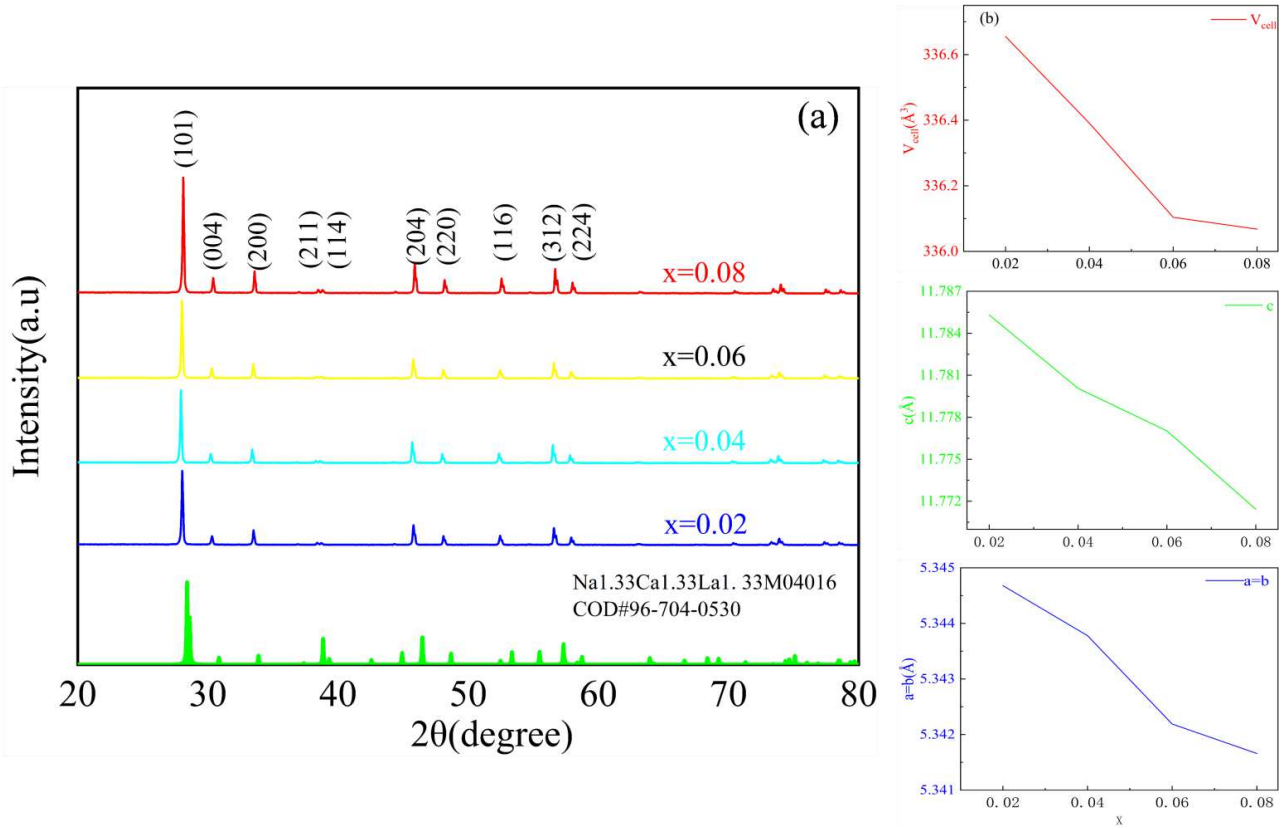


Figure 1. (a) XRD patterns of $Na(Sr_{1-x}Ca_x)CeMo_3O_{12}$ ceramics with x = 0.02–0.08 sintered at the optimal temperature of 900 ℃; (b) the volume change as a function of the substitution fraction x.

3.2. Rietveld refinement and crystal structure

The representative Rietveld refinement patterns of $Na(Sr_{1-x}Ca_x)CeMo_3O_{12}$ ceramics covering the x = 0.02–0.08 compositional range are presented in Figure 2(a-d). The experimentally measured diffraction profiles (denoted by open circles), the theoretically calculated patterns (solid lines), the residual difference curves at the bottom, and the expected Bragg reflection positions (vertical bars) are plotted in the same coordinate system for direct comparison. The excellent intensity matching between the observed and calculated datasets across the entire 2θ scanning range further verifies that all sintered samples are pure single-phase tetragonal scheelite structures. In this crystal framework, Na^+, Sr^{2+}, Ca^{2+} and Ce^{4+} cations co-occupy the 4b Wyckoff site with

eight-fold oxygen coordination, forming distorted $(Na/Sr/Ca/Ce)O_8$ polyhedra, while Mo^{6+} cations are located at the 4a Wyckoff site, surrounded by four oxygen atoms to construct isolated MoO_4 tetrahedra. The $(Na/Sr/Ca/Ce)O_8$ polyhedra are interconnected with adjacent units via edge-sharing, and the discrete MoO_4 tetrahedra further link the polyhedral backbone through corner-sharing oxygen atoms, ultimately forming a stable three-dimensional open crystal network.

Table 2 summarizes all the interionic bond length data of $Na(Sr_{1-x}Ca_x)CeMo_3O_{12}$ ceramics with different Ca doping contents, which are obtained via Rietveld structural refinement at their respective optimal sintering temperatures. The doping variable x covers the range of 0.02 to 0.08, and the refinement convergence degree of all bond length values meets the published standards for crystallographic data. As indicated by the data variation trend, the average bond lengths of three non-molybdenum-oxygen bonds, namely Na-O, Sr-O and Ce-O, decrease slightly with the increase of Ca doping content, reach a minimum value of 2.5629 Å at x = 0.06, and then show a weak rebound at x = 0.08. The overall fluctuation amplitude is less than 0.002 Å, reflecting the extremely high structural stability of the lattice framework in this system. In contrast, the average bond length of Mo1-O reaches a minimum value of 1.7365 Å at x = 0.04, which is completely consistent with the previously observed experimental results of the peak lattice ordering degree and the lowest intrinsic dielectric loss. This bond length evolution trend can directly support the mechanism interpretation of dielectric properties: the x = 0.04 component has the shortest Mo-O bond length, which corresponds to the highest Mo-O bond energy and significantly suppresses the anharmonic lattice vibration. This provides direct experimental evidence at the crystal structure level for the ultra-high Q × f value of 125265 GHz obtained by this component.

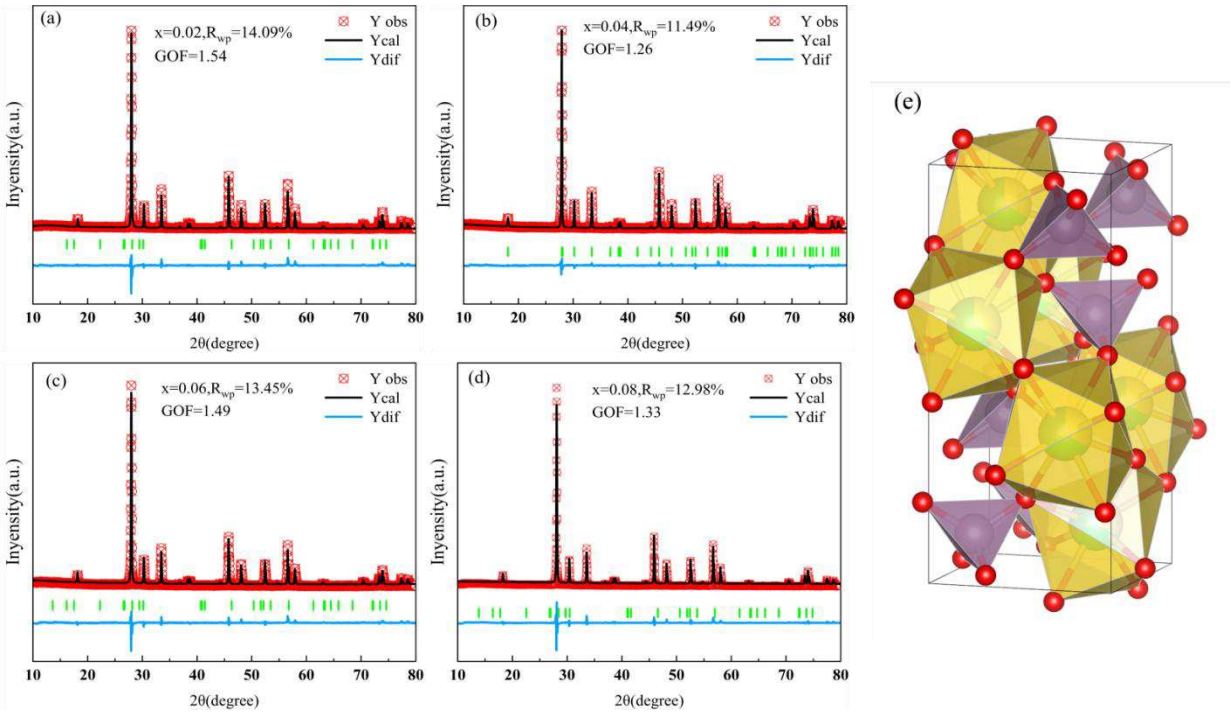


Fig. 2. (a–d) Rietveld refinement XRD patterns of $Na(Sr_{1-x}Ca_x)CeMo_3O_{12}$ (x = 0.02, 0.04, 0.06, 0.08) ceramics. (e) Crystal structure schematic and coordination polyhedra sintered at 900 ºC.

Table 1 Lattice parameters, unit cell volume, and refinement parameters of **$Na(Sr_{1-x}Ca_x)CeMo_3O_{12}$** ceramics sintered at 900°C.

$Sm_2[Zr_{1-x}(Cr_{0.5}Ta_{0.5})_x]_3[MoO_4]_9$	**V(Å3)**	**α=β(°)**	**γ (°)**	**Rp(%)**	**Rwp(%)**	**χ2**
x=0.02	336.655	5.34468	11.78531	10.668	14.090	1.54
x=0.04	336.391	5.34378	11.78007	8.287	11.489	1.26
x=0.06	336.104	5.34219	11.77703	10.427	13.453	1.49
x=0.08	335.878	5.34166	11.77143	10.834	14.034	1.44

Table 2 Bond length of the **$Na(Sr_{1-x}Ca_x)CeMo_3O_{12}$** ceramics selected at optimal sintering temperatures.

Bonds	**x=0.02**	**x=0.04**	**x=0.06**	**x=0.08**
Na-O(1)[1]×3	2.5567	2.5561	2.5554	2.5705
Na-O(2)[2]×3	2.5720	2.5711	2.5704	2.5559
Sr-O(1)[1]×3	2.5720	2.5561	2.5554	2.5705
Sr-O(2)[2]×3	2.5567	2.5711	2.5704	2.5559
Ce-O(3)[1]×3	2.5720	2.5561	2.5554	2.5705
Ce-O(3)[2]×3	2.5567	2.5711	2.5704	2.5559
Mo1-O(1)[1]	1.7192	1.7315	1.7410	1.7413
Mo1-O(2)[2]	1.7249	1.7415	1.7410	1.7413
Mo1-O(3)[3]	1.7894	1.7315	1.7410	1.7413
Mo1-O(4)[4]	1.8023	1.7415	1.7410	1.7413
Average Na-O	2.5644	2.5636	2.5629	2.5632
Average Sr-O	2.5644	2.5636	2.5629	2.5632
Average Ce-O	2.5644	2.5636	2.5629	2.5632
Average Mo1-O	1.7589	1.7365	1.7410	1.7413

3.3. Microstructure characterization

Figure 3 displays the SEM micrographs of thermally etched surfaces for $Na(Sr_{1-x}Ca_x)CeMo_3O_{12}$ ceramics sintered at 900 °C. All specimens across the compositional series reach a relatively high densification level, accompanied by a generally uniform grain size distribution throughout the entire sample set. At the substitution level x = 0.02, a certain fraction of intergranular pores still remain inside the sample, which indicates that the solid-phase sintering densification process of this specific composition has not been fully completed. As the Ca^{2+} substitution content rises to x = 0.04, the microstructure evolves into its optimal state, featuring the highest densification degree, well-distributed grain size, clearly distinguishable grain boundary profiles, and nearly no residual pores. This experimental observation shows perfect consistency with the maximum relative density value measured for this composition in Table 2. When the Ca^{2+} doping concentration is further increased to x = 0.06 and x = 0.08, the proportion of intragranular pores increases slightly, and the overall uniformity of the microstructure degrades gradually. This phenomenon can be reasonably explained by the fact that excessive Ca^{2+} substitution inhibits the lattice mass transport behavior during the high-temperature sintering process. The above microstructure evolution law shows excellent agreement with the measured relative density data, which provides a direct microscopic structural basis for the subsequent interpretation of the composition-tuned microwave dielectric property evolution mechanism.

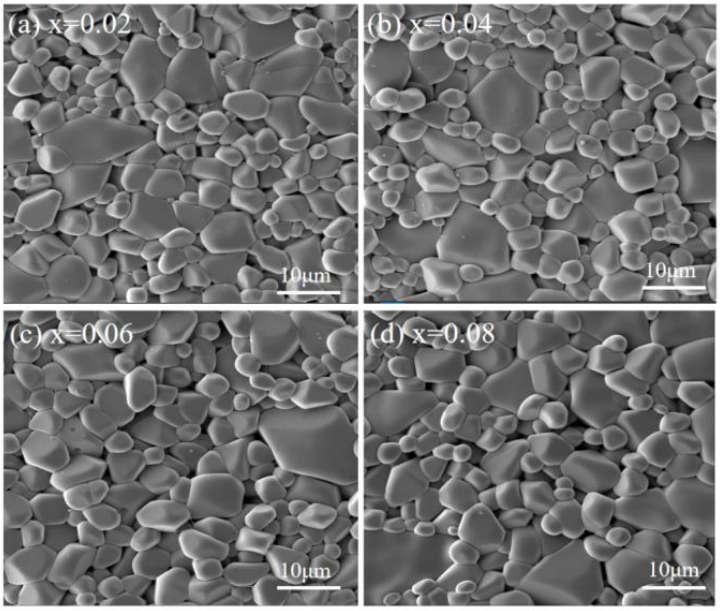


Figure 3. SEM micrographs of $Na(Sr_{1-x}Ca_x)CeMo_3O_{12}$ ceramics sintered at 900 ℃: (a) x = 0.02, (b) x = 0.04, (c) x = 0.06, (d) x = 0.08.

Figure 4 presents the statistical grain size distribution results of the same batch of ceramics sintered at 900 °C, whose evolution trend shows full consistency with the previously observed SEM morphology features. For the x = 0.02 sample, the grain size distribution spans a relatively broad interval, and a considerable number of residual pores remain trapped in the gaps between large-sized grains. The x = 0.04 sample delivers the narrowest grain size distribution range, reaching the peak grain uniformity that perfectly aligns with its highest densification level. As x further increases to 0.06 and x = 0.08, the grain size distribution broadens again, accompanied by a noticeable rebound in pore quantity and a distinct degradation in overall microstructure uniformity.

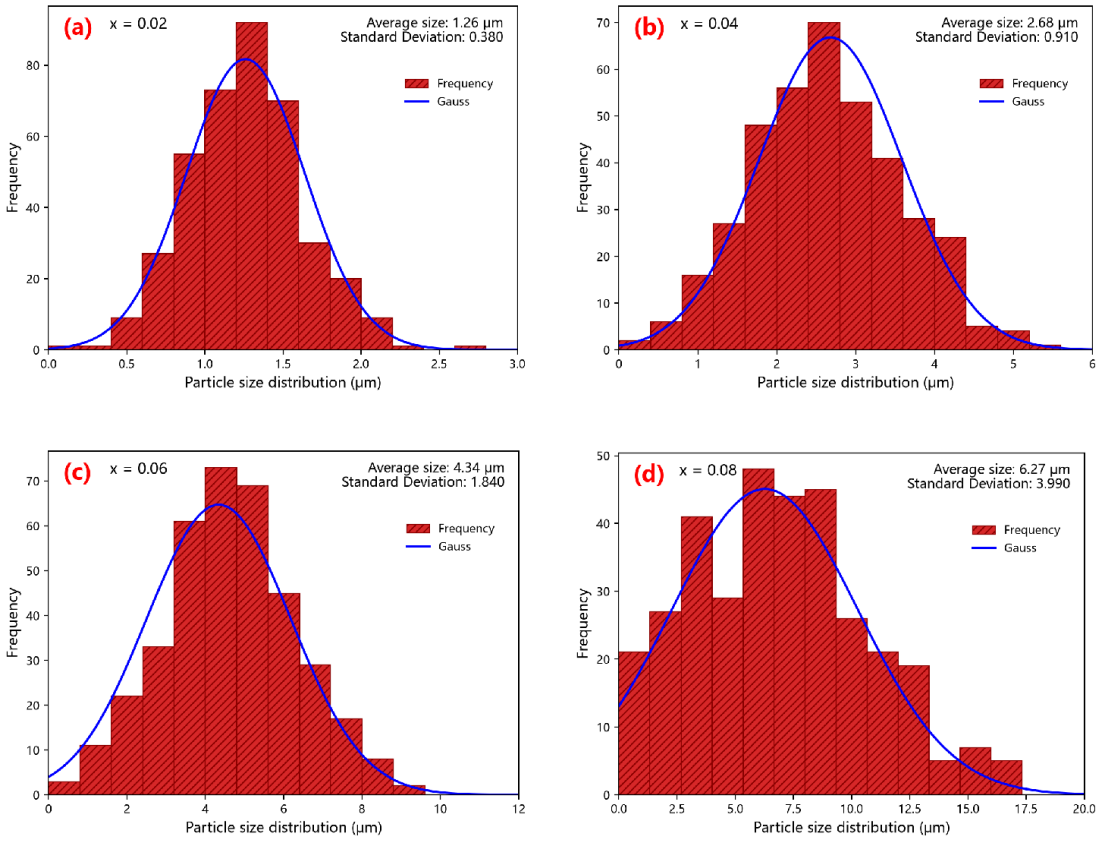


Figure 4. Ggrain size histogram of the $Na(Sr_{1-x}Ca_x)CeMo_3O_{12}$ ceramics sintered at 800°C.

Figure 5(a–d) illustrates the SEM micrographs of $Na(Sr_{0.96}Ca_{0.04})CeMo_3O_{12}$ ceramics, which capture the dynamic evolution of their microstructure as the sintering temperature gradually rises. At the sintering temperature of 850 °C, the grains have not undergone full development and growth, and a substantial number of residual pores are trapped inside the sample, indicating a distinctly insufficient densification degree. As the sintering temperature elevates to 900 °C, the pore content drops to the minimum value, the grain size reaches the highest uniformity, and the overall microstructure evolves into its optimal state. When the sintering temperature is further increased beyond this point, abnormal grain growth occurs, pores reappear within the matrix, and the structural uniformity degrades noticeably. Figure 5(e–h) presents the corresponding statistical grain size distribution results for the above morphologies, whose quantitative data further validates this temperature-driven microstructure evolution trend.

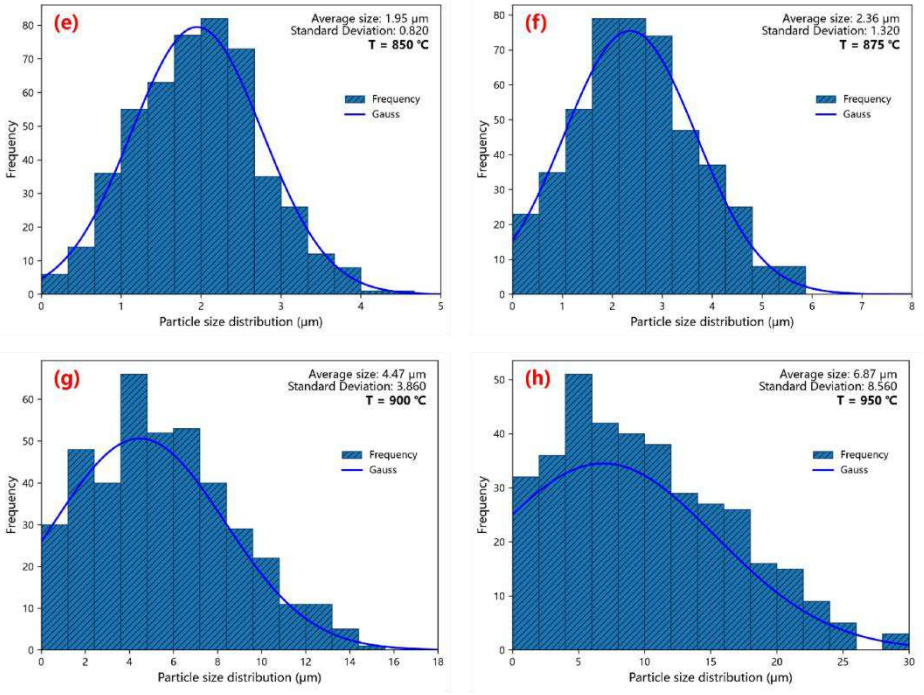


Figure 5. SEM micrographs of $Na(Sr_{0.96}Ca_{0.04})CeMo_3O_{12}$ ceramics sintered at various temperatures(Fig. 5 a-d), the average grain size (A.G.) of $Na(Sr_{0.96}Ca_{0.04})CeMo_3O_{12}$ ceramics sintered at 850-950 °C(Fig. 5 e-h).

Figure 6 presents the EDS elemental mapping patterns and corresponding quantitative compositional spectrum of the $Na(Sr_{1-x}Ca_x)CeMo_3O_{12}$ ceramic specimen sintered at 900 °C. Statistical analysis of the collected spectrum reveals that the experimentally measured atomic proportions of Na, Sr, Ca, Ce, Mo and O show excellent consistency with the nominal stoichiometric molar ratios pre-designed for this ceramic system. The minor numerical deviation between the measured and theoretical values can be reasonably attributed to the inherent instrumental sensitivity limit and unavoidable background signal calibration error that are intrinsic to the EDS characterization technique. This experimental result directly confirms the successful fabrication of the target homogeneous solid-solution phase, and no detectable elemental segregation or localized element aggregation is observed across the entire scanned region of the sample.

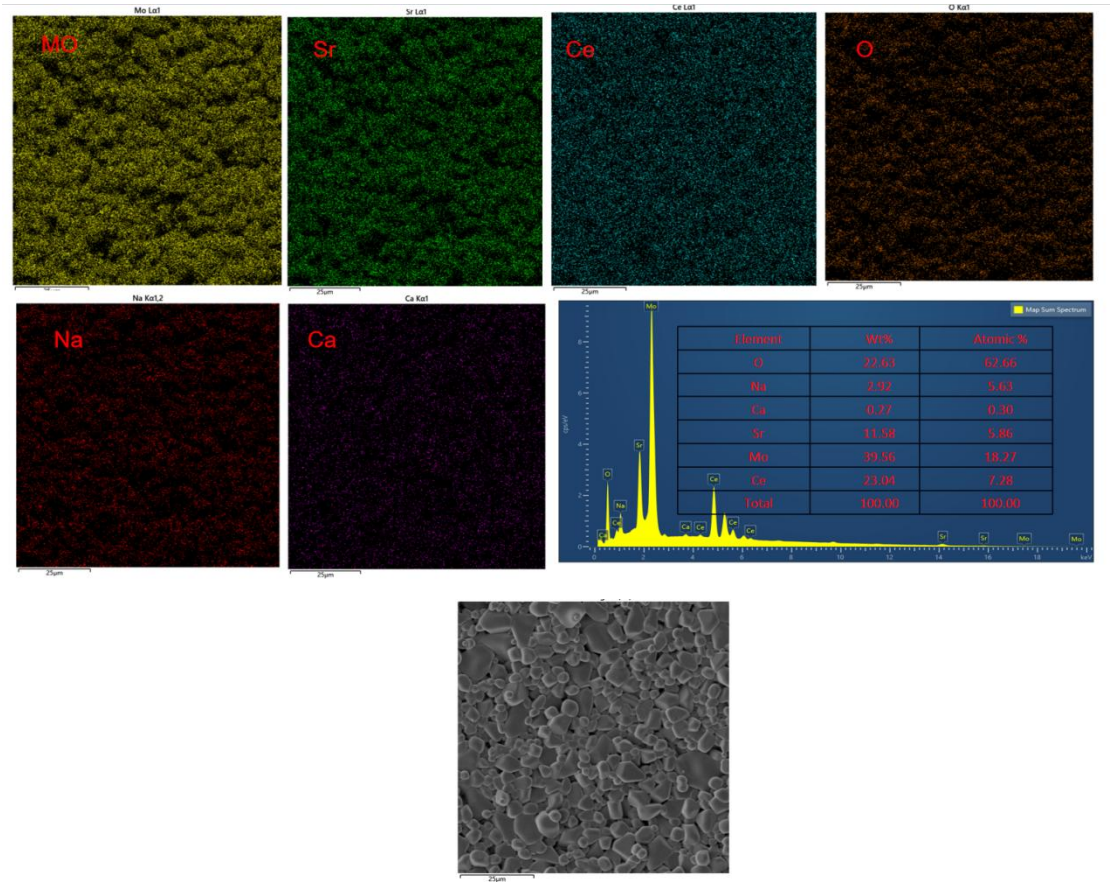


Figure. 6 shows the atomic mass ratio of $Na(Sr_{0.96}Ca_{0.04})CeMo_3O_{12}$ ceramic sintered at 900 ºC and the EDS surface scan image.

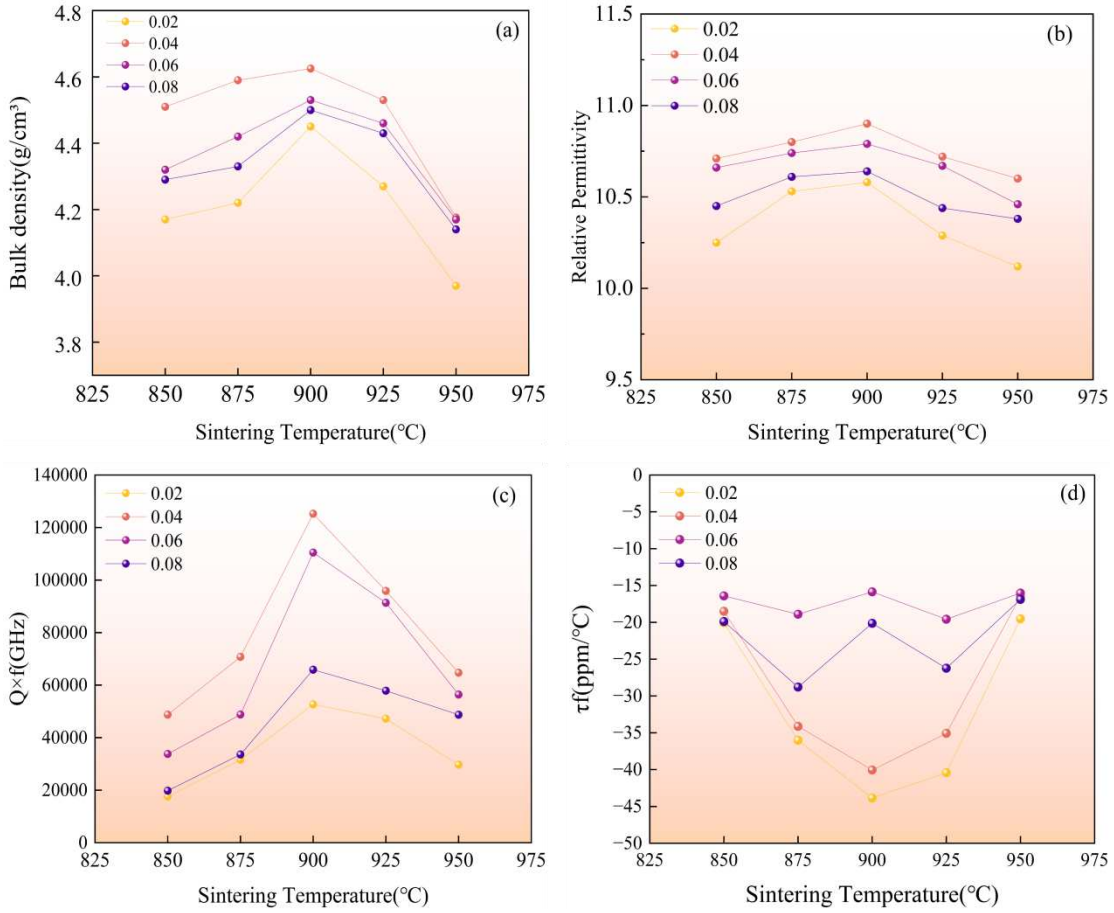


Figure 7(a) The relative density, (b) dielectric constant, (c) $Q \times f$, (d) τ_f of $Na(Sr_{1-x}Ca_x)CeMo_3O_{12}$ ceramics sintered at various temperatures.

As depicted in Figure 7(a), the relative density of Ca-doped $Na(Sr_{1-x}Ca_x)CeMo_3O_{12}$ ceramics presents a distinct non-monotonic variation trend with the increase of Ca doping concentration across the entire sintering temperature range of 850 °C to 950 °C, following an initial upward then downward trajectory: the relative density hits a peak value of roughly 4.6 g/cm³ at x = 0.04, and then undergoes a continuous decline as the Ca substitution level further rises. This phenomenon can be reasonably explained by the fact that excessive doping introduces a high concentration of lattice defects, which hinders atomic diffusion and suppresses the densification kinetics during the high-temperature sintering process. Within the full tested temperature interval, all samples sintered at 900 °C exhibit the highest densification degree, which further confirms that this temperature is the optimal processing condition to facilitate the sintering densification of this entire ceramic series.

From the intrinsic property perspective of constituent oxides, the gradual reduction in relative density induced by elevated Ca doping content can be rationally interpreted via the following physical mechanism: the melting point of CaO reaches 2572 °C, which is substantially higher than

the 2430 °C melting point of SrO. This inherent property dictates that a higher Ca substitution ratio requires a correspondingly elevated sintering temperature to drive sufficient solid-state atomic diffusion and macroscopic volume shrinkage. Under a fixed sintering temperature, a higher Ca doping concentration weakens the densification driving force throughout the sintering process, which ultimately results in a lower relative density. A higher densification degree not only promotes the enhancement of main phase purity and the suppression of secondary phase formation, but also serves as an indispensable prerequisite for securing the stability of the temperature coefficient of resonant frequency (τf).

3.4. Microwave dielectric properties

The microwave dielectric properties of $Na(Sr_{1-x}Ca_x)CeMo_3O_{12}$ ceramics sintered at their respective optimized temperatures are summarized in Table 3. The relative permittivity ε_r varies within a narrow interval of 10.58–10.90, which falls into the typical permittivity range for low-permittivity molybdate ceramics with scheelite crystal structure. In line with the Clausius–Mossotti correlation, the permittivity of a fully dense single-phase ceramic is co-determined by the theoretical total ionic polarizability (αtheo) and the unit cell volume. Since the ionic polarizability of Ca^{2+} (3.16 $Å^3$) is marginally lower than that of Sr^{2+} (4.24 $Å^3$), the normalized polarizability ratio α_{theo}/Vm remains nearly invariant as x changes, which directly explains the observed nearly constant ε_r value. The minor fluctuations in εr are predominantly correlated with the subtle variations in the bulk relative density of the sintered samples.

Figure 7(b) illustrates the variation of relative permittivity (εr) across all sintered samples prepared at different temperatures, plotted as a function of Ca substitution content (x). As x gradually increases, εr follows a distinct non-monotonic trajectory of first ascending and then descending, rising from 10.58 to a peak value of 10.90 at the substitution level x = 0.04. The initial upward trend is predominantly governed by the continuous improvement in bulk densification degree during the sintering process. Nevertheless, when x exceeds 0.04, the relative permittivity decreases progressively, which arises from the synergistic effects of reduced bulk relative density, elevated lattice defect concentration, and the inherently lower ionic polarizability of Ca^{2+} compared to Sr^{2+}. As described by the Clausius–Mossotti [17-18] correlation, the relative permittivity exhibits an intrinsic correlation with ionic polarizability, and its specific mathematical formulation is presented in the following section:

$$\varepsilon_{rtheo}=\frac{3V+8\pi\alpha_{theo}}{3V-4\pi\alpha_{theo}} \quad (2)$$

where α_{theo} denotes the theoretical ionic polarizability and V represents the molar volume of the unit cell (V/Z). The total polarizability of the compound is calculated on the basis of Shannon's additive rule for ionic polarizabilities [19], which is expressed as follows:

$$\alpha_{theo}.[Na(Sr_{1-x}Ca_x)CeMo_3O_{12}]=\alpha(Na^{+}）+(1\text{-}x)\alpha（Sr^{2+}）$$
$$+x\alpha（Ca^{2+}）+\alpha Ce^{4+}+\alpha(Mo^{6+})+\alpha（O^{2-}）$$

（3）

The Shannon ionic polarizabilities of Ca^{2+} and Sr^{2+} are well-documented as 3.16 $Å^3$ and 4.24 $Å^3$ respectively. As the Ca substitution level (x) gradually rises, the theoretical total polarizability (α_{theo}) of the entire ceramic system exhibits a monotonic downward trend. This inherent decreasing trend in total polarizability is effectively counterbalanced by the concurrent improvement in bulk relative density, which ultimately drives the observed initial upward trajectory of the measured relative permittivity (ε_r). To eliminate the confounding interference effect of residual porosity on the raw dielectric measurement data, the experimentally obtained ε_r values were corrected using the Bosman-Having relation via Equation (4), which yields the porosity-corrected relative permittivity (ε_{rcorr}) as defined in the subsequent xpression.

$$\varepsilon_{r\ corr}=\varepsilon_{r\ mea}(1+1.5p) \quad (4)$$

Where P and εr denote the porosity and experimentally measured relative permittivity respectively. Furthermore, the theoretical relative permittivity (ε_{rtheo}) of the microwave ceramics can be derived from the total ionic polarizability (α_{theo})[19], which is explicitly formulated in Equation (4). Figure 7(b) depicts the variation of experimentally measured relative permittivity (ε_r) as a function of Ca^{2+} substitution content (x), which presents a distinct non-monotonic trajectory of first ascending and then descending. Specifically, for the specimens sintered at 900 °C, the measured ε_r first climbs to a peak value, and then gradually decreases from 10.9 to 10.64 as x increases progressively. Notably, both the theoretically calculated permittivity ($\varepsilon_{r,theo}$) and the bulk relative density follow the identical declining trend as the measured εrεr in the post-peak region, which corroborates the strong intrinsic correlation among these three key performance parameters.

The quality factor Q × f exhibits a distinct composition-dependent characteristic, as clearly presented in Fig. 7(c). It increases remarkably from 52694 GHz at x = 0.02 to a peak value of 125265 GHz at x = 0.04, and then gradually declines to 65870 GHz at x = 0.08 for specimens

sintered at 900 °C. This volcano-shaped variation trend can be rationally interpreted from both extrinsic and intrinsic perspectives. Extrinsically, the sample with x = 0.04 possesses the highest relative density and the most uniform microstructure, which effectively minimizes the extrinsic dielectric loss originating from residual pores and abnormal grain boundaries. Intrinsically, the atomic packing fraction and the lattice energy of Mo–O bonds play decisive roles: an appropriate amount of Ca^{2+} substitution optimizes the Mo–O bond strength and suppresses anharmonic lattice vibration, while excessive Ca^{2+} doping introduces local lattice strain that intensifies phonon scattering. The Raman full width at half maximum (FWHM) of the A_1g mode corresponding to MoO_4 tetrahedra reaches its minimum value of 24.87 cm^{-1} at x = 0.04, which further corroborates that the optimal composition owns the highest lattice ordering degree and the lowest intrinsic dielectric loss. Fig. 7(d) intuitively depicts the variation of the temperature coefficient of resonant frequency τf for $Na(Sr_{1-x}Ca_x)CeMo_3O_{12}$ ceramics as a function of Ca^{2+} substitution content, where all tested samples were sintered at 900 °C. Across the entire substitution range, τf remains negative, covering the numerical interval of −15.864 ~ −43.855 ppm/°C. As the x value increases progressively, τf continuously shifts toward a less negative direction, and this variation trend is closely correlated with the reduction of the system's linear thermal expansion coefficient αth and the synchronous evolution of bond valence inside the crystal lattice. Although the τf value of the x = 0.06 composition in Fig. 7(d) is −15.9 ppm/°C, which still does not reach the near-zero level, it can be conveniently tuned to near-zero by constructing a composite ceramic system with a small fraction of τf-compensating end-members in subsequent studies, so as to satisfy the temperature stability requirements of practical communication devices. More importantly, the optimal ceramic composition can achieve full densification at 900 °C. This sintering temperature is far below the melting point of Ag electrodes, demonstrating extremely high application compatibility in the LTCC (Low-temperature co-fired ceramic) technology field. A systematic performance comparison between this system and other representative molybdate microwave dielectric ceramics is summarized in Table 1, Table 3 and Table 4. The comparison results highlight that the Q × f value of 125265 GHz obtained in this work reaches an exceptionally high level among all reported ultra-low-firing molybdate systems, presenting remarkable competitive performance advantages.

Table 3 Q×f, ε_r, τ_f, ε_{rtheo}, α_{theo} , ρ_{theo}, $\rho_{relative}$, S_{Mo-O}, V_{iMo-O} for $Na(Sr_{1-x}Ca_x)CeMo_3O_{12}$ (x=0.02-0.08) ceramics sintered at 900°C.

X	0.02	0.04	0.06	0.08
Q×f (GHz)	52694	125265	110467	65870
εr	10.58	10.9	10.79	10.64
τf (ppm/°C)	-43.85532	-40.05986	-15.86398	-20.13572
εrtheo	10.7529	10.7660	10.7820	10.7906
αtheo (Å³)[per cell, Z=6]	61.4640	61.4352	61.4065	61.3778
αtheo/Vm	0.1826	0.1826	0.1827	0.1827
ρtheo (g/cm³)	4.384	4.383	4.382	4.381
P (%)	9.44	4.72	4.84	5.50
U(Mo-O) (kJ/mol)	24839.63	25533.87	25438.85	25435.86
E(Mo-O) (fi)	582.53	598.56	598.73	598.63
αmn(10-6K-1)	-0.43	-0.417	-0.407	-0.407

3.5 Chemical Bond Analysis Based on P–V–L Theory

The P–V–L chemical bond theory acts as a classical analytical framework that interprets the chemical bonding behaviors in crystalline solids from the perspective of dielectric response properties. On the basis of this theoretical system, the crystal structure of $Na(Sr_{1-x}Ca_x)CeMo_3O_{12}$ ceramics can be deconstructed into multiple independent chemical bond units, which follow the general A_mB_n bond classification scheme. This targeted decomposition operation lays a solid structural foundation for the subsequent quantitative calculation of bond-related parameters and the in-depth interpretation of structure-performance correlation:

$$Na(Sr/Ca)LnMo_3O_{12} \rightarrow (Na/Sr/Ca/Ln)MoO_4 \rightarrow Na/Sr/Ca/Ln + Mo + O_4 \rightarrow Na/Sr/LnO_{8/3} + MoO_{4/3} \quad (5)$$

To quantitatively characterize the ionic-covalent dual properties of $Na(Sr_{1-x}Ca_x)CeMo_3O_{12}$ ceramics, a set of targeted calculation formulas are constructed on the basis of the P–V–L chemical

bond theory system. [21-26]:

$$f_i^{\mu}=\frac{(C^{\mu})^2}{(E_g^{\mu})^2} \quad (6)$$

$$f_c^{\mu}=\frac{(E_h^{\mu})^2}{(E_g^{\mu})^2} \quad (7)$$

$$(E_g^{\mu})^2=(E_h^{\mu})^2+(C^{\mu})^2 \quad (8)$$

$$E_h^{\mu}=39.74/(d^{\mu})^{2.48} \quad (9)$$

$$C^{\mu}=14.4b^{\mu}\exp(-\kappa_s^{\mu}r_0^{\mu})\times[\frac{m}{n}(Z_A^{\mu})^*-(Z_B^{\mu})^*]/r_0^{\mu} \quad (10)$$

where E_g^{μ} represents the average energy gap of the dielectric ceramic, and C^{μ} denotes the heteropolar energy induced by ionic bonds in the chemical bonds of the dielectric ceramic [26-30]. In the equation, E_h^{μ} indicates the homopolar energy resulting from covalent bonds in the chemical bonds of the dielectric ceramic, d^{μ}represents the bond length in the dielectric ceramic [30-36], and $(Z_A^{\mu})^*$and $(Z_B^{\mu})^*$signify the effective numbers of valence electrons for the positively charged ion A and negatively charged ion B, respectively. The parameter $b^{\mu}$is a structural correction factor positively correlated with the average coordination number N_C^u. The Thomas–Fermi screening factor $\exp(-\kappa_s^{\mu}r_0^{\mu})$ is determined as follows [37-40]:

$$\kappa_s^{\mu}=\left(\frac{4k_F^{\mu}}{\pi\alpha_B}\right)^{\frac{1}{2}} \quad (11)$$

$$(k_F^{\mu})^3=3\pi^2(N_e^{\mu})^* \quad (12)$$

$$(N_e^{\mu})^*=\frac{(n_{\mu})^*}{v_b^{\mu}} \quad (13)$$

$$(n_{\mu})^*=\frac{(Z_A)^*}{N_{cA}^{\mu}}+\frac{(Z_B)^*}{N_{cB}^{\mu}} \quad (14)$$

$$v_b^{\mu}=\frac{(d_{\mu})^3}{\sum_v(d_{\mu})^3*N_b^v} \quad (15)$$

where $\alpha_B$represents the Bohr radius, a constant with a value of 0.5292 Å. k_F^{μ}denotes the Fermi wave vector of the valence electrons, N_e^{μ}indicates the density of valence electrons in the ceramic crystal, N_b^vsignifies the bond density in the ceramic crystal, and n_{μ}represents the average number of valence electrons in the chemical bonds of the ceramic.

The bond ionicity of each independent chemical bond unit in the as-prepared ceramics was quantitatively calculated using Equation (6), and the corresponding calculation outcomes are

intuitively presented in Figure 8(a). Among all constituent chemical bonds in the crystal lattice, the Sr/Ca-O and Mo-O bonds exhibit distinctly higher ionicity than other bond units, which are identified as the dominant bonding factors that govern the macroscopic dielectric constant of the investigated ceramic samples. Nevertheless, as clearly demonstrated in Figure 8(a), the overall bond ionicity of the samples maintains a highly stable value of approximately 84.8% across the entire Ca substitution range. Consequently, in this work, the bond ionicity fi exerts a negligible influence on the variation of the measured dielectric constant, and this deduction shows excellent consistency with the experimental results presented in Figure 8.

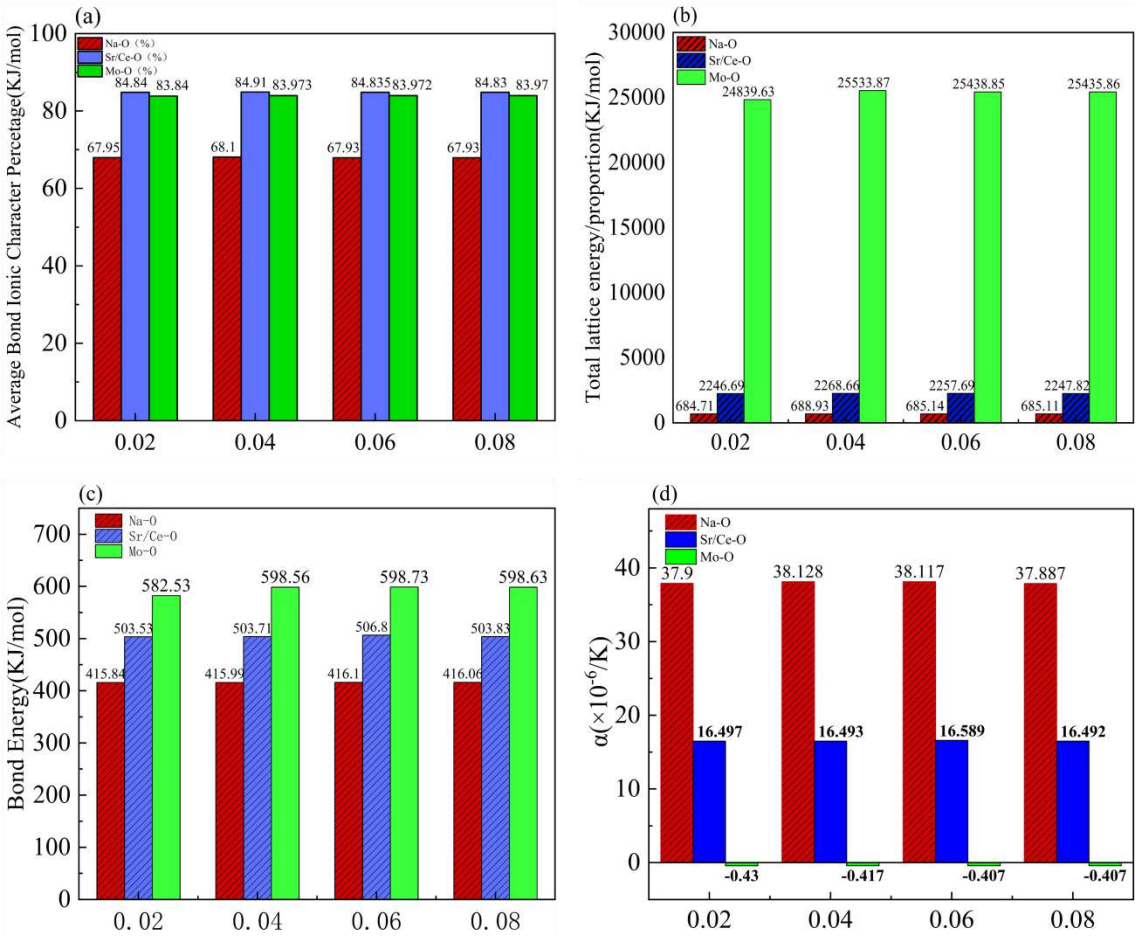


Fig. 8(a), (b), (c), and (d) respectively represent the results of Ave fi, Ave U, Total E and α_{mn} for sintered at a temperature of 900℃.

The loss characteristics of microwave dielectric ceramics act as one of the most critical evaluation indicators for their comprehensive performance. The Q×f value is universally adopted to quantitatively characterize the loss behavior of tested samples, where a higher Q×f value corresponds to lower dielectric loss level. These dielectric losses can be fundamentally divided

into two distinct categories: intrinsic loss and extrinsic loss. The intrinsic loss is inherently tied to the crystal structure, atomic packing fraction, and lattice energy (U) of chemical bonds within the crystalline lattice. In contrast, the extrinsic loss is governed by a broader set of influencing factors, including lattice defects, residual porosity, bulk material density, secondary phase formation, grain size heterogeneity, and the introduction of dopant atoms [41-42]. Figure 7(b) and Figure 8(b) systematically depict the variation of quality factor Q×f as a function of Ca doping content x in the $Na(Sr_{1-x}Ca_x)CeMo_3O_{12}$ ceramic system sintered at 900 °C, and intuitively reveal the intrinsic coupling correlations between Q×f and the lattice energy of Mo–O bonds, total lattice energy of the entire system, as well as atomic packing fraction. As the doping concentration x increases progressively, Q×f exhibits a continuous upward trend and reaches its performance peak at x = 0.04. Fully synchronized with this variation trajectory, both the total lattice energy and atomic packing fraction also hit their maximum values at this specific doping level, and the three parameters present highly consistent evolution patterns. When the doping content x exceeds 0.04, the lattice energy of Mo–O bonds, total system lattice energy and bulk density of the samples decrease synchronously, and Q×f also declines in a coordinated manner. The three parameters always maintain a perfectly matched evolutionary trend throughout the entire doping range.

This performance evolution law can be rationally interpreted from the intrinsic mechanism perspective. On one hand, higher lattice energy corresponds to stronger chemical bonding force, which can remarkably suppress the anharmonic lattice vibration and fundamentally reduce the intrinsic dielectric loss of the system. On the other hand, a higher density indicates a more compact atomic arrangement inside the crystal and superior lattice ordering, which can effectively attenuate the energy dissipation induced by phonon scattering processes. Accordingly, a stable positive correlation is established among Q×f, total lattice energy and packing fraction. These three parameters collectively verify the prominent suppression effect of the synergistic action between densified crystal structure and strong chemical bonds on intrinsic dielectric loss. Figure 7(b) illustrates the variation trend of Q×f value for $Na(Sr_{1-x}Ca_x)CeMo_3O_{12}$ ceramics as a function of sintering temperature. As the sintering temperature increases, the Q×f value presents a trend of first ascending and then descending. Combined with the data in Table 3, the relative density of samples sintered at 900 °C can exceed 95% for x=0.04 and x=0.06, which provides solid experimental support for the high Q×f characteristic of the samples. When x=0.04 and the sintering temperature is 900 °C, the Q×f value of the ceramic reaches a peak of 125265 GHz, corresponding

to the optimal loss performance of the sample. When the sintering temperature is fixed at 900 °C as shown in Figure 10(b), the Q×f value of this ceramic system gradually rises with the increase of doping content x, reaches its maximum at x=0.04 and then declines subsequently. The variation of Q×f exhibits a highly consistent trend with the lattice energy U and bulk density of the sample, while no obvious correlation is observed between Q×f and the packing fraction, which further clarifies that lattice bonding strength and densification degree are the core microscopic factors dominating the loss performance of this system.

Figure 9 (a-d) systematically correlates the experimentally measured relative permittivity (εr) of 900 °C-sintered ceramics with the ε_r(C–M) values derived from the modified Clausius–Mossotti framework. The full computational workflow supporting this comparison is formalized in Equation (16) and Equation (17), which are tailored for multi-component molybdate dielectric systems.

$$\varepsilon_r(C-M)=\frac{3}{1-\frac{b\alpha_{th}}{V_m}}-2 \tag{16}$$

$$V_m=\frac{V}{Z} \tag{17}$$

where b is a constant fixed at 4π/3, V0 represents the original unit cell volume, and VRietveld denotes the unit cell volume extracted from Rietveld refinement respectively. Z refers to the total number of atoms contained in a single unit cell. αth is defined as the theoretical polarizability of $Na(Sr_{1-x}Ca_x)CeMo_3O_{12}$ ceramics. As a core microscopic parameter that characterizes the intrinsic polarization performance of dielectric materials, it can be quantitatively calculated via the generalized Shannon formula as presented in Equation (18) [34]:

$$\alpha_{th} = \alpha(Na^{1+}) + (1-x)\alpha(Sr^{2+}) + x\alpha(Ca^{2+})+(Ce^{4+}) + 3\alpha(Mo^{6+}) + 12\alpha(O^{2-}) \tag{18}$$

Where $\alpha(Na^{1+})$, $\alpha(Sr^{2+})$, $\alpha(Ca^{2+})$, $\alpha(Ce^{4+})$, (Mo^{3+}) and $\alpha(O^{2-})$ represent the ionic polarizabilities of Na^{1+}, Ca^{2+}, Sr^{2+},Ce^{4+}, Mo^{3+} and O^{2-} ions, respectively. Their values were taken from relevant literature [34].

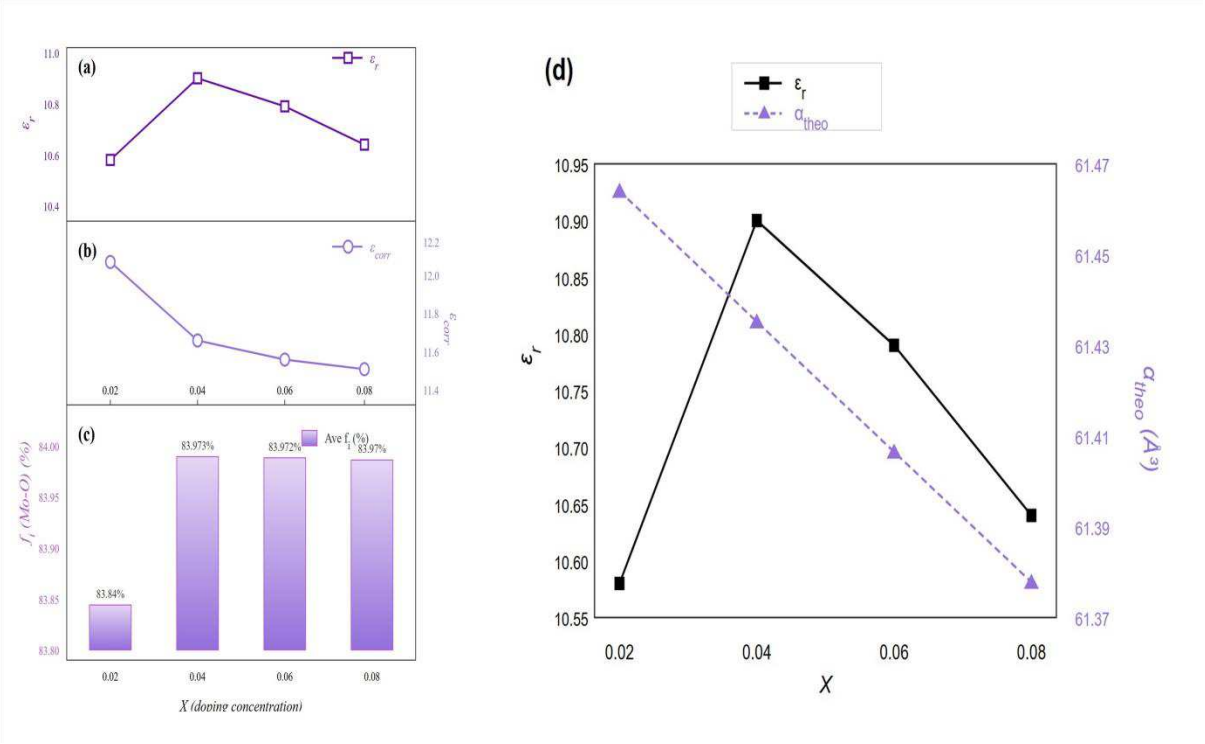


Fig. 9(a), (b), (c), and (d) respectively represent the results of ε_r, ε_{corr}, ε_r, Ave fi, α_{tho}, for $Na(Sr_{1-x}Ca_x)CeMo_3O_{12}$ sintered at a temperature of 900°C.

Estimating εr(C–M) via polarizability is a widely recognized and highly effective analytical approach. The calculated outcomes presented in Figure 9(b) demonstrate that the theoretical values share a comparable overall variation tendency with the experimentally measured counterparts. It is noteworthy that ε_{corr} consistently registers higher than the experimental measurements, which is primarily ascribed to the unavoidable residual pores existing in actual bulk samples, since the incorporation of pores effectively lowers the overall dielectric constant. Further detailed observation reveals that the variation trend of the dielectric constant exhibits a strong synchronization with that of the relative density, which fully corroborates that relative density exerts a prominent regulatory effect on the dielectric constant: the higher the densification degree, the closer the dielectric constant will approach the theoretical predicted value. The coupling relationship among dielectric constant, bond ionicity and polarizability in the $Na(Sr_{1-x}Ca_x)CeMo_3O_{12}$ ceramic system presents a distinct segmented modulation behavior, which can be precisely categorized into two typical regions corresponding to different dominant control factors. Under this circumstance, the intrinsic regulatory effect of bond ionicity and theoretical polarizability on dielectric constant can be nearly completely neglected. Instead, the variation of ε_r displays a highly synchronous evolution trend with the relative density of the sintered samples, and the gradual elimination of residual pores and continuous improvement of densification become the sole dominant factor driving the continuous rise of dielectric constant in this interval. When the doping level exceeds $x = 0.04$, the introduction of excessive Ca^{2+} disrupts the original coordination equilibrium of the lattice. The bond valence distribution of Sr/Ca-O and Mo-O bonds undergoes a noticeable deviation from the optimal stable state, which triggers a synchronous and regular decline in the total bond ionicity and theoretical polarizability of the system. In this high doping region where $x > 0.04$, the evolution of dielectric constant shows a highly consistent positive correlation with both bond ionicity and theoretical polarizability, and the intrinsic chemical bonding parameters replace relative density to become the dominant modulation factor for the variation of ε_r. This segmented evolution law clearly illustrates that the extrinsic pore effect occupies an absolutely dominant position in governing dielectric constant during the low-doping densification stage, while the alteration of intrinsic chemical bond properties turns into the core driving force for the dielectric constant evolution in the high-doping lattice distortion stage, and the synergistic action of the two mechanisms fully covers the performance evolution logic of dielectric constant across the entire Ca substitution range.

Figures 7(d) and Figure 10(c) jointly uncover the intrinsic coupling mechanism among the resonant frequency temperature coefficient τ_f, bulk bond energy, and Mo-O bond valence in the $Na(Sr_{1-x}Ca_x)CeMo_3O_{12}$ ceramic system. τ_f presents a prominent positive correlation with the overall bond energy: higher bond energy can substantially boost the intrinsic structural stability of the crystal lattice, exerting a stronger suppression effect on temperature-induced resonant frequency drift and the lattice thermal expansion coefficient α_{mn}. As a consequence, the absolute value of τ_f is notably reduced and gradually converges toward zero. Conversely, when the bulk bond energy declines, the lattice's capability to resist temperature perturbations is impaired, the absolute value of τf rises correspondingly, and the thermal stability of the material degrades remarkably. As for the Mo-O bond valence, although this work does not directly construct a quantitative mapping relationship between it and τf, the bond valence theory confirms that higher Mo-O bond valence and total system bond energy generally correspond to stronger chemical bonding strength and shorter equilibrium bond lengths, which act as the direct microscopic origins for the enhancement of bulk bond energy. Hence, the synergistic elevation of Mo-O bond valence and total system bond energy can indirectly drive a further increase in the overall bond energy of the system, ultimately lowering the absolute value of τf and effectively optimizing the resonant frequency thermal stability of the as-prepared material.

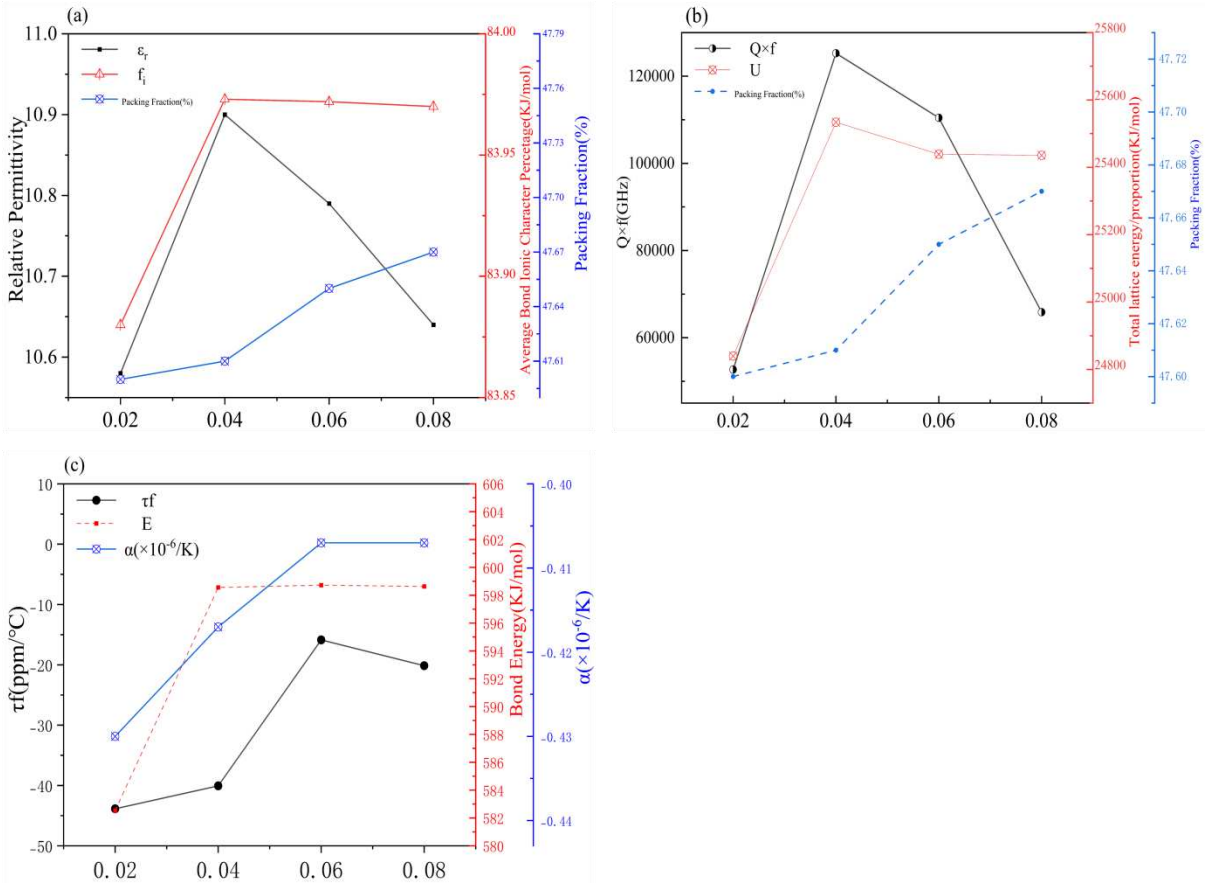


Figure 10. Trends of key parameters for $Na(Sr_{1-x}Ca_x)CeMo_3O_{12}$ ceramics (x = 0.02–0.08) sintered at 900 °C:(a) ε_r, f_i, and Packing Fraction; (b) Q×f, U, Packing fraction; (c) τ_f, Bond Enerengy(E) and α .

In summary, for the $Na(Sr_{1-x}Ca_x)CeMo_3O_{12}$ ceramic system, synchronously increasing the bond energy and Mo-O bond valence can drive both τ_f and the lattice thermal expansion coefficient αmn to converge towards zero. Consequently, the core of achieving near-zero τ_f performance in this system lies in realizing precise synergistic balance between bond energy and bond valence through component regulation.

The percentage of bond ionicity for the three types of chemical bonds consistently maintains a stable hierarchical relationship. As shown in Figure 8(a), the Sr/Ce-O bond exhibits the highest ionicity (approximately 84.84%–84.83%), which acts as the dominant bond type regulating the relative permittivity (ε_r) of the ceramic. This is followed by the Mo-O bond (approximately 83.84%–83.9772%), while the Na-O bond shows the lowest ionicity (approximately 67.93%–68.1%). The overall bond ionicity stably follows the order of Sr/Ce-O > Mo-O > Na-O. Ca doping

only exerts a weak influence on the ionicity of the Sr-O bond, and has almost no regulatory effect on the ionicity of the Mo-O and Na-O bonds. The bond with the highest ionicity is closely correlated with the ε_r value [27], while the Mo-O and Sr-O bonds with lower ionicity are the main contributors to intrinsic dielectric loss. Notably, in this system, the bond ionicity and relative permittivity do not present a completely consistent evolution trend.

Lattice energy (U) acts as a core microscopic parameter that characterizes the relative bonding strength of chemical bonds within the crystal lattice. In general, higher lattice energy corresponds to more robust crystal structure stability, which is conducive to reducing the microwave dielectric loss of the as-prepared material. As clearly presented in Figure 8(b), the lattice energy of the Mo-O bond exceeds 24835 kJ/mol, which is remarkably higher than that of all other chemical bonds in the system. This observation confirms that the Mo-O bond serves as the dominant factor governing the comprehensive performance of this ceramic system. Correlation analysis combined with the datasets in Figure 8(b) reveals a distinct positive correlation between lattice energy and the Q×f value: the elevation of lattice energy directly facilitates the improvement of Q×f, which further validates the positive regulatory effect of lattice energy on the quality factor. The specific calculation formula for lattice energy is formalized as follows [40]:

$$U_b^{\mu}=U_{bc}^{\mu}+U_{bi}^{\mu} \quad (19)$$

$$U_{bc}^{\mu}=2100m\frac{(Z_+^{\mu})^{1.64}}{(d^{\mu})^{0.75}}f_c^{\mu} \quad (20)$$

$$U_{bi}^{\mu}=1270\frac{(m+n)Z_+^{\mu}Z^{\mu}}{d^{\mu}}\left(1-\frac{0.4}{d^{\mu}}\right)f_i^{\mu} \quad (21)$$

In the equation, U_{bc}^{μ}corresponds to the covalent component of the chemical bond lattice energy in the dielectric ceramic, while U_{bi}^{μ}represents its ionic component. Z^+ and Z^- denote the valences of the positive and negative ions in the chemical bond, respectively.

As shown in Figure 8(b) and Figure 10(b), the bond lattice energy (U_b) calculated based on the P-V-L theory exhibits a positive correlation with the Q×f value: a higher U_b corresponds to a higher Q×f. For single-phase ceramics, the Q×f value is primarily dominated by intrinsic losses; generally, a more stable crystal structure yields a higher U_b, which can simultaneously reduce both the intrinsic and internal losses within the ceramic system. In this study, the initial U_b value gradually increased from 24839 kJ/mol to 25533 kJ/mol, and then decreased slowly. This variation trend is completely consistent with the evolution law of Q×f. It is worth noting that the regulation effect of U_b on Q×f exhibits a distinct segmented characteristic across different doping regions. In

the low doping region of $x < 0.04$, the moderate substitution of Ca^{2+} promotes grain boundary migration and eliminates the micropores inside the grains, leading to a continuous improvement in the relative density of the samples. Under this condition, U_b and the packing fraction increase synchronously, and both evolve in close agreement with the Q×f value, indicating that lattice energy and the densified structure synergistically dominate the suppression of intrinsic loss at this stage. When the doping level exceeds $x > 0.04$, the excessive Ca^{2+} induces local ionic site mismatch and lattice distortion, and the packing fraction decreases owing to the destruction of the close-packed atomic arrangement. Nevertheless, the bonding strength of the Mo-O bond and U_b remain the key variables determining the intrinsic loss. In this high doping region, the variation of Q×f no longer shows an obvious correlation with the packing fraction, but remains highly synchronized with U_b, which further demonstrates that lattice energy replaces densification to become the dominant controlling factor for the evolution of Q×f. In summary, lattice energy is the core dominant factor affecting the Q×f value; it acts synergistically with the packing fraction during the densification stage of $x < 0.04$, while it independently governs the evolution of Q×f in the lattice distortion stage of $x > 0.04$.

The temperature coefficient of resonant frequency (τf) serves as a key indicator of the thermal stability of the operating frequency. Its value is predominantly governed by the bond energy and the linear thermal expansion coefficient of the material. The bond energy can be quantitatively described by the following equation [41–42]:

$$E=E_c+E_i \quad (22)$$

$$t_i=\left|\frac{(S_A-S_B)}{6}\right| \quad (23)$$

$$t_c+t_i=1 \quad (24)$$

$$E_i=\frac{33200}{d} \quad (25)$$

$$Ec=\frac{(r_{cA}+r_{cB})}{d^{\mu}}(E_{A-A}E_{B-B})^{1/2} \quad (26)$$

Among these parameters, the ionic coefficient (t_i) and the covalent coefficient (t_c) are defined as the intrinsic properties of the chemical bonds in the dielectric ceramic, with their sum being constant at 1. The terms r_{cA} and r_{cB} denote the covalent radii of atoms A and B, respectively, while the bond energies E_{A-A} and E_{B-B} for the atoms within the chemical bond can be determined by referring to standard bond energy compilations [43]. Regarding Equation (20), S_A and S_B specifically represent the electronegativity values of atoms A and B.

$$\text{Packing fraction }(\%)_{Na(Sr1-xCax)CeMo3O12}=\frac{\frac{4}{3}\pi\times[r^3_{Na^{1+}}(1-x)r^3_{Sr^{2+}}+xr^3_{Ca^{2+}})+r^3_{Ce^{4+}}+3r^3_{Mo^{6+}}+1}{V_m/Z} \quad (27)$$

$$U_b^{\mu}=U_{bc}^{\mu}+U_{bi}^{\mu} \quad (28)$$

$$U_{bc}^{\mu}=2100m\frac{\left(Q_A^{\mu}\right)^{1.64}}{(d^{\mu})^{0.75}}f_c^{\mu} \quad (29)$$

$$U_{bi}^{\mu}=1270\frac{(m+n)Z_A^{\mu}Z_B^{\mu}}{d^{\mu}}\left(1-\frac{0.4}{d^{\mu}}\right)f_i^{\mu} \quad (30)$$

$U_{bi\mu}$ and $U_{bc\mu}$ represent the energy contributions of bond ionicity and bond covalency for the μ-type chemical bond, while $Z_{A\mu}$ and $Z_{B\mu}$ represent the valence states of the cation and anion[43-44].

There are numerous factors that influence the temperature coefficient of resonant frequency (τ_f), including the degree of octahedral distortion, the thermal expansion coefficient (α_L), and the total bond valence of cations.The expression of τf is as follows[44]:

$$\tau_f=-\alpha_L-\frac{\tau_\varepsilon}{2} \quad (31)$$

$$\beta_{mn}=\frac{m(m+n)}{2n} \quad (32)$$

$$\gamma_{mn}=\frac{kZ_AN_{CA}}{U_b\Delta_A}\beta_{mn} \quad (33)$$

$$\alpha_{mn}=-3.1685+0.8376\gamma_{mn} \quad (34)$$

$$\alpha_L=\sum F_{mn}\alpha_{mn} \quad (35)$$

N_{CA} represents the cation coordination number, τ_ε is the temperature coefficient of the dielectric constant, k is the Boltzmann constant, △A represents the periodic constant of the cation, and Fmn is the proportion of a single chemical bond. Liu and others used the bond valence theory to analyze the temperature coefficient of resonant frequency, which is an effective method.The expression for calculating the bond valence of $Na(Sr_{1-x}Ca_x)CeMo_3O_{12}$ ($0.02\leq x\leq 0.08$) ceramics is as follows [45]:

$$V_{total}=\sum_j V_{ij} \quad (36)$$

$$V_{ij}=\exp\left(\frac{R-d_{ij}}{b}\right) \quad (37)$$

Vtotal represents the sum of the bond valences of all chemical bonds, R represents the bond

valence parameter, which can be found in relevant literature [46-51], d_{ij} represents the bond length between atom i and atom j, and b equals 0.37Å.

Under the experimental condition of constant sintering and holding at 900 °C for 4 h, Figure 7(d) and Figure 10(c) systematically reveal the evolution law of the resonant frequency temperature coefficient (τ_f) of $Na(Sr_{1-x}Ca_x)CeMo_3O_{12}$ ceramics with the Ca doping mole fraction x, and clarify the regulation effect of different sintering temperatures on this performance evolution path. The experimental results from the two figures clearly show that as the doping content x increases gradually, the proportion of Ca^{2+} substituting for Sr^{2+} in the lattice continues to rise, and the τf parameter of the corresponding ceramic samples exhibits a significant and traceable evolution characteristic. The intrinsic origin of this performance evolution behavior can be directly attributed to the precise modulation effect of the heterovalent introduced Ca^{2+} sites on the local crystal structure and chemical bond strength of the system [35].

In the $Na(Sr_{1-x}Ca_x)CeMo_3O_{12}$ ceramic system, the simultaneous reduction of the resonant frequency temperature coefficient (τ_f) and thermal expansion coefficient after Ca^{2+} substitutes for Sr^{2+} essentially originates from the multi-dimensional synergistic regulation of intrinsic ionic properties, chemical bond characteristics and crystal structure: after Ca^{2+} with an ionic radius of 1.12 Å and far lower ionic polarizability than Sr^{2+} occupies the A-site of the lattice, the overall average ionic polarizability of the system decreases significantly, and the temperature-dependent effect of the lattice thermal vibration dipole moment is greatly suppressed, which directly weakens the drift amplitude of the dielectric constant with temperature. Combined with the strong negative correlation between τ_f and the temperature coefficient of dielectric constant, the τ_f value is finally promoted to decrease significantly and gradually converge to the near-zero range; meanwhile, the introduction of Ca^{2+} reconstructs the chemical bond distribution in the system. The Ca-O bond, whose bond strength and lattice energy are much higher than those of the original Sr-O bond, can indirectly increase the bond order of the Mo-O framework bond and strengthen the binding stability of the whole lattice. The stronger chemical bonds restrict the thermal vibration displacement of atoms during the heating process, which not only reduces the intrinsic thermal expansion coefficient of the lattice, but also decreases the temperature-induced non-uniform elongation of bond length, fundamentally inhibits the temperature offset of resonant frequency, and realizes the simultaneous decrease of τ_f and thermal expansion coefficient; in addition, appropriate amount of Ca^{2+} substitution can optimize the local distortion degree of the lattice,

significantly improve the thermal stability of the crystal structure to avoid the occurrence of unexpected phase transition during temperature change, and Ca doping can promote the densification of ceramics and reduce internal pores and other defects, further weakening the abnormal thermal expansion caused by extrinsic factors, and finally making the overall thermal expansion behavior of the material more gentle, the temperature stability of τ_f is also synchronously improved.

3.6 Raman spectrum analysis

As a direct characterization technique for lattice vibrations, Raman spectroscopy can accurately establish the intrinsic correlation between the fine crystal structure and macroscopic dielectric properties [52-53]. To date, no Raman spectroscopic studies on $Na(Sr_{1-x}Ca_x)CeMo_3O_{12}$ series ceramics have been reported in academia. This work presents the first systematic Raman characterization and analysis of the four-component ceramics, providing core experimental basis for subsequent research on the vibrational properties of this system. Except for the $Na(Sr_{1-x}Ca_x)CeMo_3O_{12}$ samples, their Raman spectra are almost completely consistent with the publicly reported spectrum of $NaSrLaMo_3O_{12}$. All ceramics in this series crystallize in a scheelite-type crystal structure with the space group of $I4_1/a$ (No. 88) and point group of C_4h (4/m). Based on the results of group theory calculation, 45 optical vibrational modes and 3 acoustic vibrational modes theoretically exist at the Brillouin zone center of this system. However, as can be seen from the experimental results in Figure 11(a), the number of Raman peaks actually observed is far less than the total number of theoretically predicted vibrational modes ($3A_g+7B_g+7E_g^1+7E_g^2$). This phenomenon can be attributed to the severe overlap of adjacent Raman peaks and the upper limit of experimental spectral resolution. As shown in Fig. 11(b), the Raman spectrum in the 200–1200 cm^{-1} region was deconvoluted into multiple Gaussian–Lorentzian components to resolve the severely overlapped vibrational modes, and a representative sample with x = 0.04 was selected for this analysis. All samples exhibited Raman spectra characteristic of compounds containing isolated $(MoO_4)^{2-}$ tetrahedral units, with a distinct Raman-silent region observed in the 500–700 cm^{-1} range that is fully consistent with the structural features of the scheelite-type crystal structure. The Raman peaks in the low-frequency region below 300 cm^{-1} are assigned to lattice vibration modes (external modes), which are primarily associated with the translational and rotational motions of $(MoO_4)^2$ groups as well as the translational vibrations of Na^+, Sr^{2+}/Ca^{2+} and Ce^{4+} cations; the

characteristic peaks in the 300–500 cm^{-1} medium-frequency interval correspond to the bending vibration modes (ν_2 and ν_4) of $(MoO_4)^{2-}$ tetrahedra, while the signals in the 700–1000 cm^{-1} high-frequency region originate from the stretching vibration modes (ν_1 and ν_3) of $(MoO_4)^{2-}$ tetrahedra, and the most intense peak located near 900 cm^{-1} corresponds to the symmetric stretching vibration mode (ν_1) of the $(MoO_4)^{2-}$ tetrahedron. There exists an intrinsic correlation between the relative permittivity εr and the Raman shift (phonon frequency ω), and this relationship can be qualitatively expressed as follows: where Ω_p, ξ, k, and E_F are defined as the plasma frequency, ionization energy, wave number, and Fermi level, respectively. This derived relationship clearly demonstrates that the relative permittivity εr exhibits an inverse proportionality to the phonon frequency ω. Accordingly, as illustrated in Fig. 11(b), the Raman shift of the ν_1 symmetric stretching mode exhibits a strong negative correlation with the gradual increase in Ca^{2+}/Sr^{2+} substitution content, the Raman shift first shifts toward the lower wavenumber side, then turns to shift toward the higher wavenumber side after the substitution content reaches x=0.04, and this variation trend shows a high degree of consistency with the evolution law of the relative permittivity.

There exists an intrinsic correlation between the relative permittivity ε_r and the Raman shift (phonon frequency ω), and this relationship can be qualitatively expressed as follows:

$$\varepsilon_r(0,\xi,k)=\frac{\Omega_p^2 \exp[\lambda(E_F^0-\xi)]}{\omega(\xi,k)} \qquad (38)$$

Here, Ωp, ξ, k, and E_F are defined as the plasma frequency, ionization energy, wave number, and Fermi level, respectively. This derived relationship clearly demonstrates that the relative permittivity ε_r exhibits an inverse proportionality to the phonon frequency ω. Accordingly, as illustrated in Figure 11(c), the Raman shift of the ν_1 symmetric stretching mode exhibits a strong negative correlation with the gradual increase in Ca^{2+}/Sr^{2+} substitution content. The Raman-active vibrations related to the $(MoO_4)^{2-}$ anionic groups can be divided into two major categories: internal vibrations and external vibrations. The signals in the high-wavenumber region correspond to the symmetric and asymmetric stretching vibrations of Mo-O bonds, and the characteristic peaks in the mid-wavenumber region are attributed to the bending vibrations of O-Mo-O bonds. In contrast, all external vibrational modes are located in the low-wavenumber region below ~250 cm^{-1}, which correspond to the translational and rotational behaviors of $(MoO_4)^{2-}$ groups and the lattice migration motions of Na^+, Sr^{2+} and Ce^{4+} cations. These vibrational modes are difficult to be accurately assigned one by one due to the strong multi-mode coupling effect. Previous studies have confirmed that the full width at half maximum (FWHM) of Raman characteristic peaks is

positively correlated with the damping degree of chemical bond vibrations, and a lower FWHM value corresponds to weaker vibration damping and lower intrinsic dielectric loss [54]. From the statistical results in Figure 11(c), Figure 11(d), it can be clearly observed that the average FWHM of Raman peaks of this series of ceramics gradually decreases with the increase of ionic radius, which directly verifies the evolution law that the intrinsic dielectric loss of the system decreases synchronously with the increase of ionic radius.

Figure 11(d) maps out the inherent linkage between the quality factor (Q×f) and the full width at half maximum (FWHM) of collected Raman peaks. The Q×f metric directly quantifies the dielectric loss performance of the as-synthesized ceramics: following the fundamental definition Q = 1/tan δ, a higher Q×f value corresponds to a lower dielectric loss tangent (tanδ). The FWHM of a Raman peak acts as a pivotal descriptor for the material's internal structural ordering, lattice defect population and phonon lifetime, and the observed peak broadening is generally driven by the combined effects of elevated structural disorder, amplified micro-defect density and enhanced lattice vibration anharmonic damping.

$$Q=\frac{1}{tan\delta}\approx\frac{\omega^2_T}{\gamma\omega}=\frac{\omega^2_T}{2\pi\gamma f} \quad (39)$$

$$\mathrm{FWHM}=\frac{\gamma\sqrt{\gamma+4\omega_0^2}}{2\omega_0} \quad (40)$$

where γ denotes the damping factor, ω_0 refers to the resonant angular frequency, and ω_T represents the vibrational frequency of the transverse optical mode within the dielectric medium. Per this derived formula, elevated lattice vibrational anharmonicity directly drives simultaneous increments in both the Raman FWHM and the dielectric loss (tanδ). This experimental observation further substantiates the well-documented negative correlation between the Q×f metric and the Raman peak FWHM as shown in Table 4. Leveraging this inherent physical linkage, the intrinsic dielectric loss behavior of the target material can be precisely assessed in a non-destructive manner. Figure 11(c) systematically maps the intrinsic correlation between Raman shift and relative permittivity (ε_r). The Raman shift directly corresponds to the characteristic vibrational frequency of lattice units: a higher wavenumber reflects elevated vibrational energy of the structural framework, which is a direct signature of enhanced chemical bond stiffness . This bond stiffness is inherently coupled to the ionic polarizability of the system. The aliovalent/iso-valent ion substitution modulates the local bonding environment: weakened bond stiffness lowers the energy barrier for ionic displacement under external alternating electric fields, which facilitates the

polarization response and elevates the macroscopic polarizability. Conversely, reinforced bond stiffness restricts the displacement of lattice ions under electric field excitation, suppressing the ionic polarization magnitude. Given the well-established positive proportionality between total ionic polarizability and macroscopic relative permittivity, the Raman shift imposes a deterministic indirect modulation on the final εr value. This quantitative correlation can be formalized via the following derived equation [38]. The inverse correlation observed between the Raman shift and the dielectric constant in the figure validates the aforementioned theoretical model. A rightward shift of the Raman peak indicates an increase in chemical bond vibration frequency and enhanced bond strength. This leads to a reduction in the polarizability of electrons and ions, accompanied by a decrease in lattice anharmonicity. Consequently, the material's polarization response to an external electric field is weakened, resulting in a decrease in the dielectric constant. This trend reflects the regulatory effect of structural densification or bond strengthening on dielectric properties, serving as a typical manifestation of the close relationship between bond strength and dielectric response.

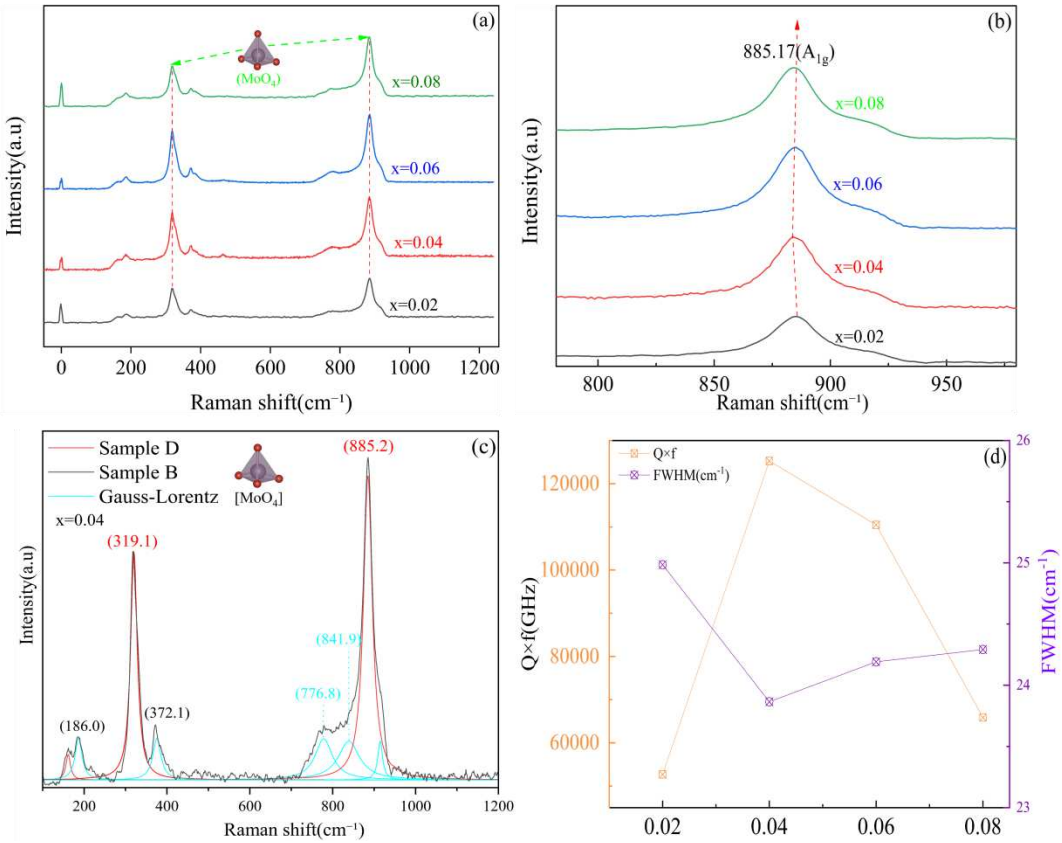


Fig. 11. Raman spectroscopy analysis for $Na(Sr_{1-x}Ca_x)CeMo_3O_{12}$ ceramics sintered at 900 °C: (a) stacked Raman spectra in the range of 100–1100 cm^{-1} with corresponding vibrational mode assignments; (b) Gaussian-Lorentzian multi-peak deconvolution in the 200–1200 cm^{-1} region for representative sample (x = 0.04); (c) magnified view of the A_1g mode shift in the 800–950 cm^{-1} range; (d) dual Y-axis plot of microwave quality factor (Q × f) and Raman FWHM as a function of substitution value x.

Table 4 . Summary of Raman spectroscopy data (A_1g mode shift and FWHM), theoretical polarizability (α_{th}), relative permittivity (ε_r), and microwave quality factor (Q × f) for **$Na(Sr_{1-x}Ca_x)CeMo_3O_{12}$** (x = 0.02–0.08) ceramics sintered at 900 °C.

Composition (x)	ST (°C)	Raman shift of A_1g (cm^{-1})	αth (Å³) [per f.u.]	αth (Å³) [per cell, Z=6]	Q × f (GHz)	FWHM of A_1g (cm^{-1})	ε_r	τ_f (ppm/°C)
0.02	900	885.17	46.1284	61.464	52694	24.985	10.58	-43.85532
0.04	900	883.76	46.1068	61.4352	125265	24.865	10.90	-40.05986
0.06	900	885.17	46.0852	61.4065	110467	24.192	10.79	-15.86398
0.08	900	885.17	46.0636	61.3778	65870	24.192	10.64	-20.13572

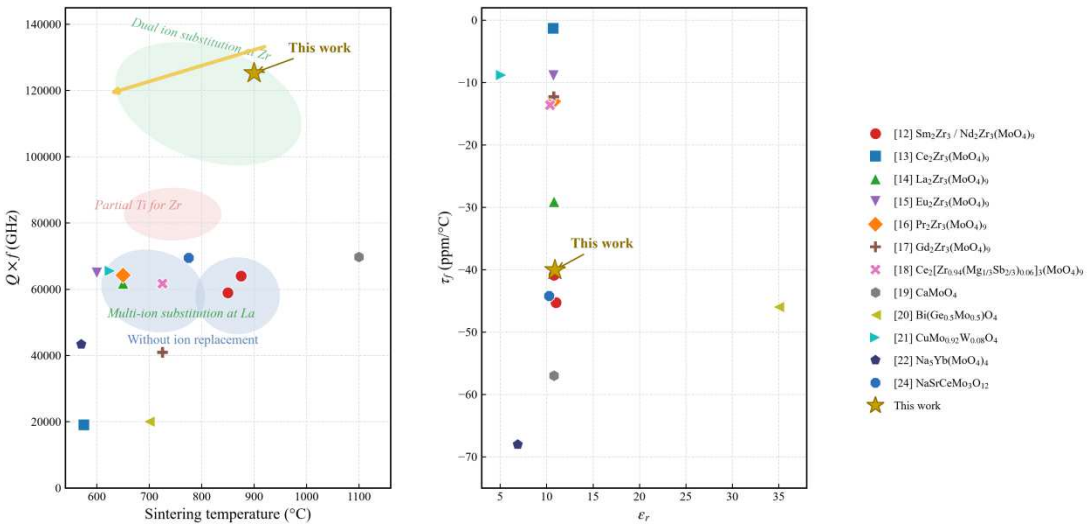


Fig. 12 Summary of microwave dielectric properties for $Na(Sr_{0.96}Ca_{0.04})CeMo_3O_{12}$ ceramics.

Figure 12. Summary of typical microwave dielectric properties of $Na(Sr_{0.96}Ca_{0.04})CeMo_3O_{12}$ ceramic sintered at 900 °C, and its horizontal performance comparison with representative reported scheelite-structured molybdate-based ultra-low-temperature co-fired ceramic (ULTCC) candidates. The optimal composition simultaneously achieves a low relative permittivity (ε_r) of 10.9, an ultra-high quality factor (Q×f) of 125,265 GHz, and a resonant frequency temperature coefficient (τf) of −40.06 ppm/°C. Notably, the Q×f value realizes a breakthrough improvement compared with the reported performance of existing molybdate ceramics in the same system, which is significantly superior to all literature samples included in the comparison. The 900 °C sintering temperature of this material is far below the melting point of Ag electrodes, showing full compatibility with Ag co-firing technology, and can be directly applied to the low-temperature co-fabrication process of millimeter-wave communication devices.

4. Conclusions

In summary, a series of novel tetragonal scheelite-structured $Na(Sr_{1-x}Ca_x)CeMo_3O_{12}$ (x = 0.02–0.08) microwave dielectric ceramics were successfully synthesized via conventional solid-state reaction, and the effects of Ca^{2+} substitution on crystal structure, densification behavior, microstructure and microwave dielectric properties were systematically investigated. The main conclusions are drawn as follows: first, XRD combined with Rietveld refinement confirms that all compositions crystallize in a single tetragonal scheelite phase (space group $I4_1/a$, No. 88; point

group C_4h, 4/m), where Ca^{2+} is incorporated into the Sr^{2+} site to form a homogeneous substitutional solid solution, and due to the smaller ionic radius of Ca^{2+} (1.12 Å) compared with Sr^{2+} (1.26 Å), the unit cell volume contracts nearly linearly from 336.655 $Å^3$ (x = 0.02) to 335.878 $Å^3$ (x = 0.08), which is in good accordance with Vegard's law; second, well-densified and homogeneous microstructures with distinct grain boundaries are obtained at a low sintering temperature of 900 °C, and the relative density increases first and then decreases with the rise of Ca^{2+} content, reaching its maximum at x = 0.04 with the lowest porosity and the most uniform grain-size distribution, while excessive substitution ($x \geq 0.06$) introduces intragranular pores and degrades microstructural uniformity; third, Ca^{2+} substitution effectively optimizes the dielectric properties, and the optimal composition at x = 0.04 simultaneously achieves a low relative permittivity (ε_r) of 10.9, a high quality factor (Q×f) of 125265 GHz and a temperature coefficient of resonant frequency (τf) of −40.06 ppm/°C, where Q×f shows a volcano-type dependence on x, and τf shifts monotonically toward the less negative direction from −43.86 to −15.86 ppm/°C as x increases; fourth, P–V–L chemical bond theory and Raman spectroscopy jointly demonstrate that the Mo–O bond plays a dominant role in determining the intrinsic dielectric loss, and the maximum Q×f at x = 0.04 originates from the synchronous maximization of Mo–O bond lattice energy and packing fraction, which effectively suppresses anharmonic lattice vibration, and the enhanced Q×f shows a strong correlation with the minimum full width at half maximum (FWHM) of the A_1g mode of the $(MoO_4)^{2-}$ tetrahedra (24.87 cm^{-1}); this work also reports the first systematic Raman characterization of this quaternary scheelite system, and the observed negative correlation between Q×f and FWHM provides a feasible non-destructive route for intrinsic dielectric loss assessment; finally, the full densification capability at 900 °C, far below the melting point of Ag electrodes (961 °C), combined with its low permittivity and high Q×f, proves that the $Na(Sr_{1-x}Ca_x)CeMo_3O_{12}$ system is a promising candidate for ultra-low-temperature co-fired ceramic (ULTCC) applications in millimeter-wave communication systems, and further tuning of τf to near-zero values via constructing composite ceramic systems will be carried out in subsequent work.

Data availability

The data that support the findings of this study are openly available to the reviewers.

Declarations

Conflict of interest The authors declare that they have no known competing financial interests or personal relationships that could have appeared to influence the work reported in this paper.

Acknowledgments

This work was financially supported by 20252112 Scientific Research Startup Fund for Introduced Talents of Taiyuan University of Science and Technology.

References

1. T.S. Rappaport, S. Sun, R. Mayzus, H. Zhao, Y. Azar, K. Wang, G.N. Wong, J.K. Schulz, M. Samimi, F. Gutierrez, Millimeter wave mobile communications for 5G cellular: It will work!, IEEE Access 1 (2013) 335–349.
2. O. Elijah, C.Y. Leow, T.A. Rahman, S. Nunoo, S.Z. Iliya, A comprehensive survey of pilot contamination in massive MIMO—5G system, IEEE Commun. Surv. Tutor. 18 (2016) 905–923.
3. I.M. Reaney, D. Iddles, Microwave dielectric ceramics for resonators and filters in mobile phone networks, J. Am. Ceram. Soc. 89 (2006) 2063–2072.
4. M.T. Sebastian, R. Ubic, H. Jantunen, Low-loss dielectric ceramic materials and their properties, Int. Mater. Rev. 60 (2015) 392–412.
5. C.–G. Gheorghe, L. Gheorghe, I. Ungurean, N. Bizon, Latency requirement for 5G mobile communications, in: Proc. 10th Int. Conf. Electron. Comput. Artif. Intell. (ECAI), Iasi, Romania, 2018, pp. 1–4.
6. W.J. Guo, X.K. Lan, Z.X. Fu, P. Liu, Structure, defects, and microwave dielectric properties of Al-doped and Al/Nd co-doped $Ba_4Nd_{9.33}Ti_{18}O_{54}$ ceramics, J. Adv. Ceram. 11 (2022) 629–640.
7. D. Zhou, L.X. Pang, D.W. Wang, I.M. Reaney, $BiVO_4$ based high k microwave dielectric materials: a review, J. Mater. Chem. C 6 (2018) 9290–9305.
8. B. Masin, J. Varghese, M.T. Sebastian, Temperature-compensated BaV_2O_6–$Ba_2V_2O_7$ ceramic composite for ULTCC applications, Ceram. Int. 48 (2022) 22479–22485.
9. Y. Imanaka, Multilayered Low Temperature Cofired Ceramics (LTCC) Technology, Springer, Boston, 2005.
10. N. Joseph, M.T. Sebastian, Glass-free $CuMoO_4$ ceramic with excellent dielectric and thermal properties for ultralow temperature cofired ceramic applications, ACS Sustain. Chem. Eng. 4 (2016) 5632–5639.
11. X. Lyu, L. Li, J. Li, W. Zhang, Sintering behavior, structure, and microwave properties of novel $Li_2Cu_{1-x}MoO_4$ ceramics, Ceram. Int. 48 (2022) 17225–17233.
12. W. Liu, R. Zuo, Low temperature fired $Ln_2Zr_3(MoO_4)_9$ (Ln = Sm, Nd) microwave dielectric ceramics, Ceram. Int. 43 (2017) 17229–17232.
13. Y. Jiang, X. Lu, C. Li, Sintering behavior, infrared spectra and microwave dielectric characteristics analysis for $Ce_2Zr_3(MoO_4)_9$ ceramics achieved by reaction-sintering method, J. Alloys Compd. 875 (2021) 160096.
14. C. Xing, H. Wu, Y. Chen, Crystal structure, infrared spectra and microwave dielectric properties of low-firing $La_2Zr_3(MoO_4)_9$ ceramics prepared by reaction-sintering process, Ceram. Int. 45 (2019) 22376–22382.
15. Y.H. Zhang, L. Li, J. Bao, Crystal structure, infrared spectra and microwave dielectric properties of novel extra-low temperature fired $Eu_2Zr_3(MoO_4)_9$ ceramics, J. Eur. Ceram. Soc. 39 (2019) 1127–1131.
16. J. Zheng, X. Wu, Y. Tang, Structure, infrared reflectivity spectra and microwave dielectric properties of a low-firing microwave dielectric ceramic $Pr_2Zr_3(MoO_4)_9$, J. Alloys Compd. 826 (2020) 153893.
17. C.F. Xing, Y. Li, H. Pan, Crystal structure, infrared spectra and microwave dielectric properties of a novel low-firing $Gd_2Zr_3(MoO_4)_9$ ceramic, Ceram. Int. 45 (2019) 22207–22214.
18. X. Zhou, L. Liu, J. Sun, N. Zhang, H. Sun, H. Wu, W. Tao, Effects of $(Mg_{1/3}Sb_{2/3})^{4+}$ substitution on the structure and microwave dielectric properties of $Ce_2Zr_3(MoO_4)_9$ ceramics, J. Adv. Ceram. 10 (2021) 778–789.
19. M. Zang, M. Zheng, M. Zhu, Y. Hou, Low-temperature sintering and microwave dielectric properties of $CaMoO_4$ ceramics for LTCC and ULTCC applications, J. Eur. Ceram. Soc. 44 (2024) 293–301.
20. D. Xu, H. Zhang, L. Pang, F. Hussain, T. Zhou, S.–K. Sun, Z. Chen, D. Zhou, Novel B-site scheelite structure ceramic $Bi(Ge_{0.5}Mo_{0.5})O_4$ and its dielectric properties, J. Am. Ceram. Soc. 106 (2023) 6675–6683.
21. L. Ren, J. Li, W. Zhang, W^{6+} doped $CuMoO_4$ ceramics with low dielectric permittivity and near-zero temperature coefficient of resonant frequency for ULTCC application, J. Eur. Ceram. Soc. 45 (2025) 116986.

22. D. Johnson, M.T. Sebastian, R. Ubic, Synthesis and characterization of $Na_5M(MoO_4)_4$ (M = Y, Yb) microwave ceramics for ULTCC applications, Ceram. Int. 44 (2018) 6699–6704.

23. J. Bao, Y. Yuan, Y. Zhang, Y. Yang, Crystal structure, Raman spectrum, bond characteristics, and terahertz time-domain spectrum of novel $Na_5Tm(MoO_4)_4$ microwave dielectric ceramic with ultra-low sintering temperature and high quality factor, J. Alloys Compd. 939 (2023) 168652.

24. X. Xu, X. Zhou, H. Wu, Y. Shi, Y. Zhang, Bonding characteristics, electrical and microwave/terahertz dielectric properties of novel tetragonal scheelite structure $NaSrLnMo_3O_{12}$ (Ln = Ce, Pr, Eu, Y, Yb) ceramics for antenna application, J. Adv. Ceram. 14 (2025) 9221179.

25. X. Xu, K. Xu, Y. Su, Y. Chen, W. Shen, C. Yuan, H. Wu, X. Zhou, J. Zhang, Ultra-low-loss $Na(Sr_{1-x}Ba_x)YbMo_3O_{12}$ ceramics: A comprehensive study on structure–property relationships and millimeter-wave device integration, Ceram. Int. 52 (2026) 4948–4962.

26. B.W. Hakki, P.D. Coleman, A dielectric resonator method of measuring inductive capacities in the millimeter range, IRE Trans. Microw. Theory Tech. 8 (1960) 402–410.

27. R.D. Shannon, Dielectric polarizabilities of ions in oxides and fluorides, J. Appl. Phys. 73 (1993) 348–366.

28. S.J. Penn, N.M. Alford, A. Templeton, X. Wang, M. Xu, M. Reece, K. Schrapel, Effect of porosity and grain size on the microwave dielectric properties of sintered alumina, J. Am. Ceram. Soc. 80 (1997) 1885–1888.

29. G. Gouadec, P. Colomban, Raman spectroscopy of nanomaterials: how spectra relate to disorder, particle size and mechanical properties, Prog. Cryst. Growth Charact. Mater. 53 (2007) 1–56.

30. J.C. Phillips, Ionicity of the chemical bond in crystals, Rev. Mod. Phys. 42 (1970) 317–356.

31. J.A. Van Vechten, Quantum dielectric theory of electronegativity in covalent systems. I. Electronic dielectric constant, Phys. Rev. 182 (1969) 891–905.

32. B.F. Levine, Bond susceptibilities and ionicities in complex crystal structures, J. Chem. Phys. 59 (1973) 1463–1486.

33. B.F. Levine, Bond-charge calculation of nonlinear optical susceptibilities for various crystal structures, Phys. Rev. B 7 (1973) 2600–2626.

34. H.Y. Yang, S.R. Zhang, H.C. Yang, E.Z. Li, Usage of P–V–L bond theory in studying the structural/property regulation of microwave dielectric ceramics: a review, Inorg. Chem. Front. 7 (2020) 4711–4753.

35. Z.J. Wu, Q.B. Meng, S.Y. Zhang, Semiempirical study on the valences of Cu and bond covalency in $Y_{1-x}Ca_xBa_2Cu_3O_{6+\gamma}$, Phys. Rev. B 58 (1998) 958–962.

36. S.S. Batsanov, Dielectric methods of studying the chemical bond and the concept of electronegativity, Russ. Chem. Rev. 51 (1982) 684–697.

37. R.D. Shannon, Revised effective ionic radii and systematic studies of interatomic distances in halides and chalcogenides, Acta Crystallogr. A 32 (1976) 751–767.

38. Y.R. Luo, Comprehensive Handbook of Chemical Bond Energies, CRC Press, Boca Raton, FL, 2007.

39. A.J. Bosman, E.E. Havinga, Temperature dependence of dielectric constants of cubic ionic compounds, Phys. Rev. 129 (1963) 1593–1600.

40. H.T. Wu, E.S. Kim, Correlation between structure and microwave dielectric properties of high-Q materials in rock-salt structure Li_2O–MgO–BO_2 (B = Ti, Sn, Zr) systems at microwave frequency, RSC Adv. 6 (2016) 47443–47453.

41. I.D. Brown, D. Altermatt, Bond-valence parameters obtained from a systematic analysis of the Inorganic Crystal Structure Database, Acta Crystallogr. B 41 (1985) 244–247.

42. N.E. Brese, M. O'Keeffe, Bond-valence parameters for solids, Acta Crystallogr. B 47 (1991) 192–197.

43. I.D. Brown, The Chemical Bond in Inorganic Chemistry: The Bond Valence Model, Oxford University Press,

Oxford, 2002.

44. Y. Tang, J. Li, H.C. Xiang, W.S. Fang, H.X. Lin, J.F. Yang, L. Fang, Rattling effect: a new mechanism affecting the resonant frequency temperature coefficient of microwave dielectric ceramics, J. Inorg. Mater. 40 (2025) 656–666.
45. E.S. Kim, B.S. Chun, R. Freer, R.J. Cernik, Effects of packing fraction and bond valence on microwave dielectric properties of $A^{2+}B^{6+}O_4$ (A^{2+}: Ca, Pb, Ba; B^{6+}: Mo, W) ceramics, J. Eur. Ceram. Soc. 30 (2010) 1731–1736.
46. H.C. Yang, S.R. Zhang, H.Y. Yang, Y. Yuan, E.Z. Li, Vibrational spectroscopic and crystal chemical analyses of double perovskite $YMgTi_2O_6$ microwave dielectric ceramics, J. Am. Ceram. Soc. 103 (2020) 1121–1130.
47. H.Y. Yang, S.R. Zhang, Y.W. Chen, H.C. Yang, Y. Yuan, E.Z. Li, Crystal chemistry, Raman spectra, and bond characteristics of trirutile-type $Co_{0.5}Ti_{0.5}TaO_4$ microwave dielectric ceramics, Inorg. Chem. 58 (2019) 968–976.
48. W. Hayes, R. Loudon, Scattering of Light by Crystals, Wiley, New York, 1978.
49. R. Loudon, The Raman effect in crystals, Adv. Phys. 13 (1964) 423–482.
50. D.L. Rousseau, R.P. Bauman, S.P.S. Porto, Normal mode determination in crystals, J. Raman Spectrosc. 10 (1981) 253–290.
51. C. Xing, J.Z. Li, J. Wang, H.T. Wu, Internal relations between crystal structures and intrinsic properties of nonstoichiometric $Ba_{1+x}MoO_4$ ceramics, Inorg. Chem. 57 (2018) 7121–7128.
52. R. Ratheesh, H. Sreemoolanadhan, M.T. Sebastian, Vibrational analysis of $Ba_{5-x}Sr_xNb_4O_{15}$ microwave dielectric ceramic resonators, J. Solid State Chem. 131 (1997) 192–195.
53. M. Balkanski, R.F. Wallis, E. Haro, Anharmonic effects in light scattering due to optical phonons in silicon, Phys. Rev. B 28 (1983) 1928–1934.
54. P.G. Klemens, Anharmonic damping of optical phonons, Phys. Rev. 148 (1966) 845–848.